

Design, Fabrication and Control of Micro-Actuators for Dual-Stage Servo Systems in Magnetic Disk Files

Roberto Horowitz, Tsung-Lin Chen, Kenn Oldham, and Yunfeng Li

Computer Mechanics Laboratory (CML)

Department of Mechanical Engineering

University of California at Berkeley, CA 94720-1740

1 Introduction

Since the first hard disk drive (HDD) was invented in the 1950s by IBM, disk drives' storage density has been following Moore's law, doubling roughly every 18 months. The current storage density is 10 million times larger than that of the first HDD (Yamaguchi, 2001). Historically, increases in storage density have been achieved by almost equal increases in track density, the number of tracks encircling the disk, and bit density, the number of bits in each track. However, because of superparamagnetism limitations, it is predicted that future areal storage density increases in HDDs will be achieved mainly through an increase in track density (Howell *et al.*, 1999).

Research of the HDD industry is now targeting an areal density of one terabit per square inch. For a predicted bit aspect ratio of 4:1, this translates to a linear bit density of 2M bits per inch (BPI), and a radial track density of 500K tracks per inch (TPI), which in turn implies a track width of 50 nm. A simple rule of thumb for servo design in HDDs is that three times the statistical standard deviation of the position error between the head and the center of the data track should be less than 1/10 of the track width. Thus, nanometer-level precision of the servo system will be required to achieve such a storage density.

A disk drive stores data as magnetic patterns, forming bits, on one or more disks. The polarity of each bit is detected (read) or set (written) by an electromagnetic device known as the read/write head. The job of a disk drive's servo system is to position the read/write head over the bits to be read or written as they spin by on the disk. In a conventional disk drive, this is done by sweeping over the disk a long arm consisting of a voice coil motor (VCM), an E-block, suspensions, and sliders, as shown in Figs. 1 and 2. A read/write head is fabricated on the edge of each slider (one for each disk surface). Each slider is supported by a suspension and flies over the surface of disk on an air-bearing. The VCM actuates the suspensions and sliders about a pivot in the center of the E-block. This operation is described in more detail in the following section.

[Figure 1 about here.]

[Figure 2 about here.]

The key to increasing HDD servo precision is to increase servo control bandwidth. However, the bandwidth of a traditional single-stage servo system as shown in Fig. 2 is limited by the multiple mechanical resonance modes of the pivot, the E-block,

and the suspension between the VCM and the head. Nonlinear friction of the pivot bearing also limits achievable servo precision. Dual-stage actuation, with a second stage actuator placed between the VCM and the head, has been proposed as a solution that would increase servo bandwidth and servo precision.

Several different secondary actuation forces and configurations have been proposed, each having strengths and weaknesses given the requirements of HDDs. The dual-stage configurations can be categorized into three groups: actuated suspension, actuated slider and actuated head. Within these, actuation forces include piezoelectric, electrostatic, and electromagnetic. In this chapter, design, fabrication and control of an electrostatic MEMS microactuator (MA) for actuated slider dual-stage positioning are discussed.

2 Design of the Electrostatic Microactuator

2.1 Disk drive structural requirements

The servo system of a hard disk drive is the mechatronic device that locates and reads data on the disk. In essence, it is a large arm that sweeps across the surface of the disk. At the end of the arm is the read-write head, containing the magnetic reading and writing elements that transfer information to and from the disk. This read-write head is contained in a box-like structure known as a slider. The slider has a contoured lower surface that acts as an air bearing between the head and the disk. The high-velocity airflow generated by the spinning disk pushes up on the air-bearing surface, maintaining the slider and read-write head at a constant distance from the disk, despite unevenness of the disk, permitting reliable data reading and writing.

The arm over an HDD's disk has three primary stages: the voice-coil motor (VCM), the e-block, and the the suspension. In a conventional disk drive, the voice-coil motor performs all positioning of the head, swinging it back and forth across the disk. The E-block lies between the VCM and the suspension and contains the pivot point. The suspension projects from the E-block over the disk as a thin flexible structure, generally narrowing to a point at the location of the slider.

For a disk drive servo to operate effectively, it must maintain the read-write head at a precise height above the disk surface and within a narrow range between the disk tracks that are arranged in concentric circles around the disk. It must also be able to seek from one track on the disk to another. Information about the track the head is following is encoded in sectors that radiate out from center of the disk, allowing the head to identify its position and distance from the center of the track. To maintain a correct flying height, the suspension must be designed with an appropriate stiffness in the vertical direction to balance an air-bearing force corresponding to the slider design in use in the drive. Meanwhile, the suspension must be flexible to roll and pitch at the slider location to permit adaptation to unevenness of the disk surface. This is accomplished using a gimbal structure. The suspension as a whole, however, should not be able to bend or twist, as this would misdirect the head, away from the track it is following.

As data densities in HDDs increase and track widths diminish, single-stage, conventional servo systems become less able to successfully position the head. Because the voice coil/E-block/suspension assembly is large and massive as a unit, the speed

at which the head can be controlled is limited. Furthermore, the assembly tends to have a low natural frequency, which can accentuate vibration in the disk drive and cause off-track errors. At track densities approaching one Terabit per square inch, the vibration induced by airflow in a disk drive alone is enough to force the head off-track.

A solution to these problems is to complement the VCM with a smaller, second actuator to form a dual-stage servo system. The VCM continues to provide rough positioning, while the second actuator does fine positioning and damps out vibration and other disturbances. The smaller second actuator can typically be designed to have a much higher natural frequency and less susceptibility to vibration than the VCM. Any actuator used in a dual-stage system should be inexpensive to build, require little power to operate, and preserve the stiffness properties described above necessary to maintain the flying height.

2.2 Dual-stage servo configurations

In the past six years, much research work has been dedicated to the exploration of suitable secondary actuators for constructing dual-stage servo systems for HDDs. A number of different secondary actuation forces and configurations have been proposed, each of which has strengths and weaknesses given the requirements of HDDs. These dual-stage configurations can be categorized into three groups: “actuated suspension”, “actuated slider” and “actuated head”.

Actuated suspension: In this approach, the suspension is re-designed to accommodate an active component, typically a piezoelectric material. This piezoelectric material stretches or flexes the suspension to position the slider and magnetic head. Piezoelectric material is an active actuation element that produces a large actuation force but small actuation stroke. Therefore, in the “actuated-suspension” configuration, the piezoelectric actuators are usually implemented in a leverage mechanism that can convert small actuation displacements into large head displacements. Typically, this places the piezoelectric actuators away from the magnetic head (between the E-block and suspension) so that they can have a long leverage arm to produce a sufficient magnetic-head motion. The advantage of this approach is that the suspension can be fabricated by a conventional suspension-making process, and its dual-stage servo configuration is effective in attaining low frequency runout attenuation in the positioning servo loop. The major drawback of this approach is that the system is still susceptible to instabilities due to the excitation of suspension resonance modes. Thus, track-per-inch (TPI) servo performance can be increased, but remains limited when compared to the alternative two approaches. Nonetheless, this approach is expected to be the first to be deployed in commercial HDDs (R.B. Evans and Messner, 1999) (I. Naniwa and Sato, 1999)

Actuated slider: In this approach, a microactuator is placed between the slider and gimbal to position the slider/magnetic heads. The resulting servo bandwidth of this approach can be higher than the previous one because the secondary actuation bypasses the mechanical resonances of the suspension. This approach uses existing sliders and microactuators that can be batch fabricated, and thus could be cost effective. However, the size and mass of the microactuator is significant relative to that of current sliders and may interfere with the slider flying stability. Therefore, current suspensions need to be re-designed to adopt this secondary actuator. Suitable driving forces in this approach include electrostatic, electromagnetic and piezoelectric (Horsley, 1998) (Muller, 2000) (Koganezawa *et al.*, 1997) (Fan *et al.*, 1999). To further reduce the assembly task of placing the

microactuator in between gimbal structure and slider, some researchers have proposed microactuators that are either integrated with the gimbal structure (Muller, 2000) or the slider (Imamura *et al.*, 1998).

Actuated head: In this approach, the slider is re-designed so that the microactuators can be placed inside the slider block and actuate the magnetic heads with respect to the rest of the slider body. As these microactuators are very small, they only slightly increase the slider weight, and are thus capable of working with the current suspension assembly. Researchers have successfully demonstrated the integrated fabrication process for fabricating the electrostatic microactuators and magnetic heads within one piece of ceramic block (slider). The embedded electrostatic microactuator has its resonance close to 30 KHz and was able to position the magnetic heads relative to the rest of the slider body by $0.5 \mu\text{m}$ (Imamura *et al.*, 1996) (Nakamura *et al.*, 1999). Full-fledged integration of slider, actuator, and read/write head remains a challenge.

In this chapter, we focus on actuated slider configurations, as they involve a great deal of interesting micro-scale engineering. In particular, we will discuss electrostatic actuation, which is probably the most common method of implementing microactuation in microelectromechanical devices. Any such microactuator will exhibit certain features:

- a fixed base, which attaches to the suspension
- a movable slider mounting point, upon which the slider rests
- springs between the base and platform, flexible in the direction of desired motion, and stiff in all other directions
- an electrostatic actuation array that generates the force used to move the platform and slider.

Microactuators must also include a wiring scheme for transferring signals to and from the slider, and often incorporate a structure for sensing the motion of the slider relative to the suspension. Electrostatic microactuators to be discussed in this chapter include hexSil and DRIE fabricated actuators from the University of California, Berkeley and electroplating-formed actuators by IBM and the University of Tokyo.

Alternatives to electrostatic actuation in an actuated slider configuration are electromagnetic or piezoelectric force. Electromagnetic microactuators use ferromagnetic films to produce a force perpendicular to an applied electric field. This type of actuation has potentially low voltage requirements but requires special fabrication techniques to integrate the magnetic components into the assembly. A microactuator of this type for hard disk drives is under development at Seagate, with results as yet unpublished. Piezoelectric microactuators use a piezoelectric material, which expands or contracts in response to applied voltage, to move the slider. These actuators have simple fabrication, the patterning a piece of piezoelectric material to sit between the suspension and slider, but it is difficult to obtain an adequate range of motion. A short stroke from the piezoelectric piece must be leveraged into a much larger motion at the read/write head. A piezoelectric microactuator has been produced by TDK corporation with a $0.5 \mu\text{m}$ stroke length at 10 V, with a 10 V bias (Soeno *et al.*, 1999).

2.3 Electrostatic microactuators: Comb-drives vs. Parallel-plates

Electrostatic microactuators have been studied as the secondary actuators in HDDs for their relative ease of fabrication, particularly in the configurations of "Actuated slider" and "Actuated head", since the structural material need only be conductive, rather than ferromagnetic or piezoelectric. Electrostatic force is generated by applying a voltage difference between the moving shuttle and a fixed stator element. Depending on the designated motion for the shuttle, electrostatic actuators are often categorized into two groups: comb-drives and parallel-plates, as illustrated in Fig. 3.

[Figure 3 about here.]

The magnitude of the electrostatic force generated equals the rate of change of energy that is retained within the finger-like structure and varied by shuttle motion. Therefore, the electrostatic force for comb-drives actuators, in which the designated shuttle motion moves along the x-direction, as shown in Fig. 3, equals

$$F_{comb} = \frac{\partial E}{\partial x} = \frac{\epsilon h}{2d} V^2, \quad (1)$$

where ϵ is the permittivity of air, x is the overlap for two plates, h is plate thickness and d is the gap between two parallel plates. Similarly, the electrostatic force for parallel-plates actuators is,

$$F_{parallel} = \frac{\partial E}{\partial y} = \frac{\epsilon x h}{2d^2} V^2 \quad (2)$$

As indicated in Eqs. (1) and (2), the electrostatic force for comb-drives actuators does not depend on the displacement of the moving shuttle and thus allows a long stroke while maintaining a constant electrostatic force. The electrostatic force for parallel-plates actuators, in contrast, is a nonlinear function of shuttle motion ($\propto 1/d^2$), and the maximum stroke is limited by the nominal gap between shuttle and stator. A longer stroke is achieved with a larger gap, at the expense of lower electrostatic force. For applications that require small stroke but large force output, parallel-plates actuators are preferred since the output force from parallel-plates can be x/d times larger than the force from comb-drives. The following equation Eq. (3) is easily derived from Eqs. (1) and (2).

$$\frac{F_{parallel}}{F_{comb}} = \frac{x}{d} \quad (3)$$

A simplified second-order differential equation is often utilized to describe the dynamic response of an electrostatic microactuator.

$$m\ddot{x}(t) + b\dot{x}(t) + K_m x(t) = F(V, x(t)), \quad (4)$$

where m is the mass of the moving shuttle, b is the damping coefficient of the microactuator, K_m is the spring constant of the mechanical spring that connects the moving shuttle to an anchor point and F is the electrostatic force that can be obtained from Eqs. (1) and (2).

2.3.1 Differential drives

Because electrostatic force is always attractive, electrostatic microactuators need other features to actively control the direction of shuttle motion in servo applications, as opposed to relying on the restoring force from a mechanical spring. For this reason, the differential-drives approach, as shown in Fig. 4, is frequently adopted in electrostatic microactuator designs. Based on the differential-drive configuration, the simplified second-order differential equation Eq. (4) is rewritten as,

$$m\ddot{x}(t) + b\dot{x}(t) + K_m x(t) = F(V_{bias} + V_{dr}, x_o - x(t)) - F(V_{bias} - V_{dr}, x_o + x(t)), \quad (5)$$

where x_o is the nominal position of the moving shuttle. If the differential drive is operated at the bias voltage (V_{bias}) with a small perturbation voltage (V_{dr}), the nonlinear force input in Eq. (5) can be linearized with a first-order approximation.

$$\begin{aligned} m\ddot{x}(t) + b\dot{x}(t) + (K_m - K_e)x(t) &= K_v V_{dr} \\ K_e &= 2 \frac{\partial F}{\partial x} \Big|_{V_{bias}} \\ K_v &= 2 \frac{\partial F}{\partial V_{dr}} \Big|_{V_{bias}}, \end{aligned} \quad (6)$$

Here, K_e represents a softening electrostatic spring constant and K_v represents the voltage-to-force gain. The electrostatic spring constant acts as a negative spring during the electrostatic microactuator operation and its value varies with the bias voltage (V_{bias}). When the electrostatic spring constant K_e exceeds the spring constant K_m from the mechanical spring, the microactuator becomes unstable; this is often described as pull-in instability. As shown in Eqs. (5) and (6), the differential configuration cancels the even order harmonics in voltage and thus linearizes the voltage–force relation to some extent. Furthermore, in parallel-plates actuators, the differential configuration reduces the nonlinearity in actuation voltage as well as in shuttle displacement.

[Figure 4 about here.]

2.3.2 Electrical isolation

Because electrostatic actuation requires multiple voltage levels for actuation force and position sensing (as discussed in the following section), electrical isolation is another challenge for designing an electrostatic microactuator. Generally speaking, when multiple voltage levels are needed in MEMS devices, electrical isolation is achieved by breaking up the parts that need to be on different voltage level and anchoring them separately to a non-conductive substrate. This approach has many drawbacks, not only because it requires a substrate in a device but also because structures have to be mechanically separated to be electrically isolated. The electrical isolation problem is far more severe in parallel-plates microactuators than comb-drive microactuators since parallel-plates actuation generally requires different voltage levels for stator fingers pulling in opposite directions.

Fig. 4 shows an example of how an electrical-isolation feature can be utilized to increase the actuation force output in a differential parallel-plates microactuator design. As shown in the figure, without the proper electrical isolation, drive-electrodes that have different voltage potentials have to be placed in separate groups, and result in the same voltage difference across

drive-electrodes and shuttle on both sides of each shuttle finger (Muller, 2000)(Horsley, 1998). Since electrostatic forces are always attractive, gaps on two sides of the interlaced structure cannot be made equal; otherwise the forces on two sides of a shuttle finger will be equal and the shuttle's movement direction will be uncontrollable. With electrical-isolation features, such as the "isolation plug", shown on the left in Fig. 4, gaps of the interlaced structure can be the same width, since different voltages can be applied on the two sides of the shuttle fingers. As shown in Fig. 4, the design with integrated electrical-isolation features is more compact than without isolation features. Consequently, more finger structures fit in the same amount of space, and actuation voltage can be reduced.

2.4 Position sensing

Most proposed HDD dual-stage servo controllers utilize only the position of the magnetic head relative to the center of data track, known in the industry as the position error signal, or PES, for closed-loop track following control. These systems have a single-input-multi-output (SIMO) control architecture. However, in some instances, it is also possible to measure the relative position error signal (RPES) of the magnetic head relative to the VCM. In this case, the control architecture is multi-input-multi-output (MIMO). As shown in (Li and Horowitz, 2001), RPES can be used in a MIMO controller to damp out the second stage actuator's resonance mode and enhance the overall robustness of the servo system.

Capacitive position sensing and piezoresistive position sensing are two popular sensing mechanisms among electrostatic microactuator designs. Each of these sensing mechanisms is discussed in more detail in the following sections.

2.4.1 Capacitive position sensing

[Figure 5 about here.]

Capacitive position sensing is based on shuttle movement causing a capacitance change between the moving shuttle and fixed stators. By measuring the change in capacitance, it is possible to determine the shuttle location relative to the fixed stator. The output voltage (V_o) for both differential drives in Fig. 5 equals $2 \delta C/C_i V_s$. The capacitance change due to shuttle movement (dC/dx) can be derived and the output voltage (V_o) for the comb-drives and parallel-plates can be formulated as a function of shuttle displacement.

$$\begin{aligned}
 V_{comb} &= 2 \frac{C_s}{C_i} \frac{\delta x}{x_0} V_s \\
 V_{parallel} &= 2 \frac{C_s}{C_i} \frac{y_0 \delta y}{y_0 - \delta y} V_s \\
 &\approx 2 \frac{C_s}{C_i} \frac{\delta y}{y_0} V_s,
 \end{aligned} \tag{7}$$

where x_0 is the nominal overlap for interlaced fingers and y_0 is the nominal gap between overlapped fingers, as shown in Fig. 5.

As indicated by Eq. (7), the voltage output for comb-drives sensing structure, V_{comb} , is linear with shuttle displacement. On the other hand, the sensing configuration that makes use of parallel-plates motion has better sensitivity for detecting shuttle motion since y_0 is usually smaller than x_0 . Although the nonlinearity in parallel-plates sensing can be linearized by the differential drive configuration to some extent, in a design example of $4\ \mu\text{m}$ gap with $1\ \mu\text{m}$ stroke, the linear model shown in Eq. (7) still produces 6% deviation from the nonlinear model.

Among electrostatic microactuators that use capacitive position sensing, the capacitance variation due to shuttle motion (dC/dx) is typically at the level of $100\text{fF}/\mu\text{m}$. In order to obtain 10 nm position sensing resolution, the capacitance sensing circuit must be able to detect capacitance variation of 1 fF in the presence of parasitic capacitance and offset/mismatches from op-amps, which can easily result in an output voltage orders of magnitude larger than the output voltage from the designated capacitance variation. In most capacitance sensing, the limiting factor for sensing resolution is not thermal noise but sensing circuit design.

[Figure 6 about here.]

Here we introduce two basic capacitance sensing circuits that are suitable for high-resolution position sensing (Wongkomet, 1998). The concept of the “synchronous scheme”, as shown in Fig. 6, is to reduce the impedance of sense capacitors as well as the offset and $1/f$ noises from op-amps by applying modulation techniques on the sense voltage (V_s). The R_{dc} resistor on the feedback loop sets the DC voltage level at the input nodes of the “charge integrator”. The effect of the presence of parasitic capacitance (C_p) is nulled out by the virtual ground condition from the op-amps. The major drawback of the synchronous scheme is that the DC-setting resistor (R_{dc}) has to be large to ensure the proper gain for the capacitance sensing (Wongkomet, 1998), which introduces excessive thermal noise into the sensing circuit. In addition, a large resistor usually consumes a large die space in implementation.

A switched-capacitance scheme, as shown at the bottom in Fig. 6, is one alternative that avoids the use of DC-setting resistor. The capacitance sensing period is broken into two phases: reset phase and sense phase. During the reset phase, input/output nodes of capacitors and input voltage to op-amps are set to ground or reference level to ensure proper DC voltage for the charge integrator. During the sense phase, sense voltage $\pm V_s$ is applied to the sense capacitors and the amount of charge proportional to the mismatch in the sense capacitors is integrated on the capacitor C_i , thus producing an output voltage that is proportional to the capacitance mismatch from the sense capacitors. This approach replaces the large DC-setting resistor by capacitors and switches and results in a much smaller die compared to the synchronous scheme. Furthermore, the switching technique allows more design flexibility for system integration and performance improvement because of the ability to allocate separate phases for various operations. The major drawback of this design is that it draws noise into sensing circuits from switches and sampling capacitor C_h . However, these noises can be compensated by dividing the sense phase into 2 ~ 3 sub-sense phases (Wongkomet, 1998), at the expense of a complicated circuit design.

2.4.2 Piezoresistive sensing

Piezoresistive films have been widely used as strain-sensitive components in a variety of MEMS devices, including pressure sensors and vibration sensors. Generally speaking, piezoresistive sensing techniques require less complicated sensing circuits and perform better in a severe environment than other sensing techniques. When a piezoresistive film is subjected to stress, the film resistivity and dimensions change. The fractional change of resistance is proportional to the deformation of the piezoresistive film. For a small change of resistance, this relation can be expressed as,

$$\frac{\Delta R}{R} = K \cdot \epsilon \quad (8)$$

where R is resistance of the piezoresistive film, K is its gage factor and ϵ is strain. In microactuator designs, the piezoresistive film is usually applied to the spring structure which connects the moving shuttle to an anchor point. When the shuttle moves, it stretches the spring as well as the piezoresistive film, consequently, the piezoresistive film produces a deformation signal that is proportional to the shuttle displacements. As a result, piezoresistive sensing is easier to implement than capacitive position sensing, but the sensing resolution is usually less accurate due to higher thermal noises introduced by the resistance of the piezoresistive film.

Another application of piezoresistive sensing, aside from measuring relative slider position, is to detect vibration in the suspension itself. The idea is to sense airflow-induced vibration of the suspension and feed that information forward to an actuated slider to damp out motion at the head. Piezoresistors used for this purpose can be made from metal or semiconductor materials, arranged as a strip or series of strips oriented along the direction of vibration strain. It is important that these sensors observe all vibration modes that contribute to off-track error, so a number of optimization schemes for locating the sensors have been developed (Hac and Liu, 1993). One method is to maximize the minimum eigenvalue of the observability matrix of the sensor or sensors. This ensures that all relevant modes are observed. Another method is to minimize a linear quadratic gaussian control problem over potential sensor locations (Hiramoto *et al.*, 2000). This serves to determine an optimal placement from the perspective of a linear controller.

2.5 Electrostatic microactuator designs for disk drives

Various electrostatic microactuators have been designed for secondary actuation in HDDs. To incorporate an electrostatic microactuator into a HDD without altering much of current suspension configuration, many design constraints are imposed. In this section, we will first discuss some design issues and then present one specific design example.

2.5.1 Translational microactuators vs. rotary microactuators

[Figure 7 about here.]

Depending on the motion of the magnetic head actuated by the microactuator, microactuator designs are categorized into two groups: translational actuators and rotary actuators. Either type can be implemented by comb-drives (Fan *et al.*, 1999) (Cheung

et al., 1996) or parallel-plates (Horsley, 1998) (Muller, 2000) (Chen *et al.*, 2002) actuation.

When employing a translational microactuator in a dual-stage HDD servo, previous research (Li and Horowitz, 2001) has shown that there exists a force coupling between the suspension and the translational microactuator, consisting of transmitted actuation force from the VCM and suspension vibration induced by windage. The force coupling from the VCM not only complicates the dual-stage servo controller but also imposes a design constraint on a translational microactuator design, in that the translational microactuator has to provide a large force output to counterbalance the coupling force. When the VCM makes a large movement, as in seeking out a new data track, the microactuator may be overpowered. One solution is to pull the actuator to one side and lock it momentarily in place. Even then, the use of the two actuation-stages must be carefully coordinated to moderate the influence of the VCM on the microactuator. On the other hand, the linear springs in the translational microactuator can also aid in damping out motion of the suspension. The portion of suspension vibration induced by windage mostly consists of high frequency excitation, so the resulting magnetic head's position error can be passively attenuated by low resonant frequency translational microactuators.

Generally speaking, rotary actuators are more difficult to design/analyze than translational actuators because of their non-uniform gap between shuttle and stator. Still, their different operating properties have both strengths and weaknesses. Unlike a translational actuator, there is no obvious force coupling transmitted from the suspension to a rotary actuator, as the microactuator is nearly always attached to the end of suspension at the microactuator's center of rotation, which acts as a pivot point. With no mechanical coupling, the dual-stage servo system using a rotary microactuator does not suffer from the force coupling between VCM and microactuator seen in translational designs. However, the rotary microactuator has to compensate for the magnetic head's position error induced by suspension vibration without any passive attenuation of the vibration. Overall, a rotary actuator is likely to behave better during track seeking and worse during track following than a translational microactuator.

2.5.2 Gimballed microactuator design

Proper flying height and orientation of a slider and read-write head over a hard disk is maintained by the interaction of the suspension, the air bearing of the slider, and a gimbal structure. The gimbal structure is located at the tip of the suspension and holds the slider/microactuator in its center coupon. The dynamic characteristic requirements of gimbal structures are that they be flexible in pitch and roll motion but stiff in in-plane and out-of-plane bending motion. To meet all these requirements using only one piece of metal is a highly challenging task. For this reason, most commercially available suspension/gimbal designs consist of two to four pieces of steel, each with different thickness.

The goal of a gimballed microactuator design is to seamlessly integrate an actuator and gimbal into a one-piece structure, as shown in Fig. 7, to simplify both suspension design and HDD assembly. A full integrated suspension that includes suspension, gimbal and microactuators in one part has also been proposed (Chen, 2001). The dimple structure, existing in most current gimbal structures, is excluded from the gimballed microactuator design and electrical interconnects are in-situ fabricated on the

gimballed microactuator, replacing the flexible cable in current HDD suspension assembly.

The dimple structure in current suspension assemblies provides out-of-plane stiffness while preserving the necessary torsional compliance in the gimbal structure. Without a dimple structure in the suspension assembly, the gimbal itself must provide high out-of-plane bending stiffness. Otherwise, it would unbalance the suspension pre-load, which is an overbend of the suspension that balances the upward air-bearing force on the suspension during operation. The electrical interconnects are implemented to transmit data between magnetic heads, located at the center coupon of the gimbal structure, and IC circuits located at the end of the suspension. The in-situ fabricated electrical interconnects are inevitably passed through torsion bars of the gimbal and thus set a design constrain for the minimum width of torsional bars. Furthermore, both the gimbal structure and microactuator should be the same thickness in order to simplify the MEMS fabrication process.

To sum up the design constrains discussed above, the integrated gimbal structure has to meet performance requirements with a single, uniform piece of material that would previously have been achieved by two to four metal pieces with different thicknesses, while the minimum width of any torsion bars that may be used pre-determined. To solve this problem, Muller (Muller, 2000) proposed a T-shaped structure (a beam structure with overhang surface sheet) for the torsion bars and Chen (Chen, 2001) proposed "double-flexured" torsion bars. Additionally, many suspension manufacturers have developed new gimbal structures for their suspensions that are designed specifically for use with MEMS microactuators, moving the gimbal location back to the suspension from the microactuator.

2.5.3 An electrostatic microactuator design example

[Figure 8 about here.]

Fig. 8 shows a translational microactuator design suitable for the HDD dual-stage actuation by Horsley in 1998 (Horsley, 1998). The translational electrostatic microactuator dimensions are $2.2\text{mm} \times 2.0\text{mm} \times 0.045\text{mm}$ and weight $67 \mu\text{g}$. The dimensions of the pico-slider on the top are $1.2\text{mm} \times 1.0\text{mm} \times 0.3\text{mm}$ and weight 1.6mg . This microactuator design does not include "electrical-isolation" features and thus the electrical isolation and electrical-interconnects were fabricated on a separate substrate and subsequently bonded to the microactuator. This microactuator uses parallel-plates for actuation force but does not have dedicated position sensing structures due to fabrication process limitation. Table 1 summarizes key parameters of this microactuator design.

[Table 1 about here.]

Based on these parameters, the characteristics of this electrostatic microactuator can be estimated by the linear differential equation shown in Eq. (6).

[Figure 9 about here.]

Fig. 9 shows the schematics of a circuit design by Wongkomet in 1998 (Wongkomet, 1998), in which actuation driving voltage and capacitive position sensing were implemented for the electrostatic microactuator designed by Horsley 1998. As mentioned before, the electrostatic microactuator design doesn't have dedicated structure for a position sensing; as a consequence, the input nodes for actuation and output nodes for capacitive position sensing have to share the same electrodes. Capacitors C_c and C_{c0} , shown in Fig. 9, are carefully designed to shield the high voltage presented in actuation circuit from sensing circuit, which is mostly low voltage, and thus enable driving/sensing circuit integration.

The driving circuit, shown in the left in Fig. 9, shows how to generate the bias voltage (V_{bias} , +/- 40V) and drive voltage (V_{dr} , -40~+40V) from the a 0~5V CMOS compatible circuits. The switches at the output of charge pumps were synchronized with the switching period ϕ_{RS} . Therefore, during the sense phases ϕ_{SN1} and ϕ_{SN2} , the switches are left open and thus no voltage fluctuation is seen by the sensing circuits. This arrangement was utilized to reduce feedthrough from the driving circuit to position sensing circuit.

The design target for the capacitive position sensing circuit was to achieve position sensing resolution of 10nm, and this goal was approached by two main techniques implemented in the circuit: differential sensing and Correlated-Double-Sampling (CDS). The main benefits of the differential sensing scheme are reduced noise coupling and feedthrough, elimination of even-order harmonics, and improvement of dynamic range by doubling the output swing. To adapt this differential sensing scheme in a differential parallel-plates electrostatic microactuator, a bias voltage (V_{bias}) was applied to the stator and the drive voltage (V_{dr}) was applied to the shuttle. The Correlated-Double-Sampling (CDS) technique, a modified capacitance sensing technique based on the switched-capacitance scheme, was implemented along with the differential sensing scheme to compensate for sensing noises including $1/f$, KT/C , switch charge injection and offset from op-amps (Wongkomet, 1998). The concepts of CDS can be briefly described as follows: The sense period is broken into 3 phases: one reset phase, ϕ_{RS} , and two sense phases, ϕ_{SN1} and ϕ_{SN2} . During the ϕ_{RS} sense phase, the voltages for capacitors and input nodes to op-amps are set to the reference level of the DC-voltage setting for the charge integrator, same as for the switched-capacitance scheme discussed in section 2.4.1. During the ϕ_{SN1} sense phase, a sensing voltage $-V_s$ is applied to the shuttle and results in a voltage difference, $\alpha(-V_s) + V_{error}$, across the sampling capacitor C_h , where α is the transfer function from sense voltage to the output voltage at the pre-amplifier, shown as $Gain$ in the plot, and V_{error} is the voltage at the output node of pre-amplifier resulting from noise, leakage charge and offset of op-amps. Lastly, during the ϕ_{SN2} sense phase, the sensing voltage is switched from $-V_s$ to V_s and the switch next to C_h is switched open. This results in a voltage output $\alpha(V_s) + V_{error}$ at the output node of the pre-amplifier and a voltage, $2\alpha(V_s)$, at the input node of the buffer. As a consequence, the voltage resulting from sensing error (V_{error}), which appears at the output node of pre-amplifier, disappears from the voltage-input node to the buffer. Switches utilized in the circuit and their correspondent timing are shown in Fig. 9. Be aware that components in the pre-amplifier and buffer are not shown in detail in Fig. 9 for presentation simplicity.

[Figure 10 about here.]

The frequency response, both open-loop and closed-loop with a PD controller, of the electrostatic microactuator measured by

a capacitive position sensing circuit is shown in Fig. 10. The position measurements from an LDV are also shown in the same plot for comparison. The deviation between measurements from the different position sensing devices, appears in the high frequency region at the plot, and has been identified as the feedthrough from the capacitance sensing circuit. The effect from feedthrough was negligible at low frequency region but becomes significant and results in a deviation in magnitude for the transfer function of $-80 \text{ dB} \sim -90 \text{ dB}$ after 2 KHz. The feedthrough presented in the capacitance sensing circuits limited the position sensing resolution to the level of 10nm.

3 Fabrication

3.1 Basic Requirements

While there are several approaches to building electrostatic microactuators suitable for hard disk drives, they all exhibit certain common features from a fabrication standpoint. As discussed earlier, nearly all electrostatic microactuators rely on a system of interlaced fingers or plates to provide actuation force. As a result, a method for producing arrays of these fingers or plates with narrow gaps between them is usually the central concern in developing a fabrication process. The resulting structure must then be strong enough to support both the slider on the microactuator and the microactuator on the suspension, particularly when loaded by the air-bearing that supports the slider above the hard drive's spinning disk. In addition, a way of performing electrical interconnection on the microactuator must be included in the design and fabrication process. This involves transferring signals to and from the actuator and slider, and isolating the parts of the microactuator requiring different voltage levels.

Additionally, the microfabrication process is subject to certain basic constraints. The materials used in fabrication must either be thermally and chemically compatible with any processing steps that take place after their deposition, or somehow protected during steps that would damage them. This often constrains the choice of materials, deposition techniques, and processing order for many microdevices. Another concern is that the surface of the structure be planar within photoresist spinning capabilities and lithography depth-of-focus limits if patterning is to be performed. This can be a major challenge for disk drive microactuators, which are large in size and feature high-aspect ratio trenches compared to other MEMS devices.

3.2 Electrostatic microactuator fabrication example

Section 2.5.3 described the design and operation of a translational electrostatic microactuator. This section examines the fabrication process by which that microactuator was built (Horsley, 1998). The process is a variation on a micro-molding process known as HexSil (Keller and Howe, 1997). In a micro-molding process, a mold wafer defines the structure of the microactuator, and may be re-used many times like dies in macro-scale molding; in the HexSil version of the procedure, the moving parts of the microactuator are formed in the mold by polysilicon. A second wafer is used to create metallized, patterned target dies. Upon extraction from the mold, the hexSil structure is bonded to this target substrate, which is patterned to determine which sections of the hexSil structure are electrically connected.

[Figure 11 about here.]

Naturally, the mold wafer is the first item to be processed, and is quite simple. The mold wafer is simply a negative image of the desired structure, etched down into the wafer's surface, as shown in figure 11a. A deep but very straight etch is critical to successful fabrication and subsequent operation of the devices. If the trench is too badly bowed or is undercut, the finished devices will become stuck in the mold. On the other hand, a tall device will have a larger electrostatic array area and will generate more force, and be better able to support a slider while in a disk drive.

Fabrication of the HexSil structure forms the majority of the processing sequence (figure 11b-g). HexSil fabrication begins by coating the surface of the mold wafer with a sacrificial silicon oxide. This layer, deposited by low-pressure chemical vapor deposition (LPCVD), must coat all surfaces of the mold, so that removal of the oxide at the end of the process will leave the device completely free of the mold. This microactuator uses a 3 to 4 μm thick oxide layer to be sure of clearance between the polysilicon structure and the trench walls during release. The mold is then refilled completely with LVPCD polysilicon, which will form the hexSil structure. Polysilicon is chosen for its conductivity and good conformality in refilling trenches. This also leaves a planar surface ready for photolithography to cover bonding locations. After the lithography step, the polysilicon deposited on top of wafer is removed, except where the bonding points were defined.

The structure is then prepared for bonding by forming a soldering surface. First, a chrome/copper seed layer is evaporated on the surface of the wafer. The chrome promotes copper adhesion to the silicon, while the copper forms the starting point for electroplating. The seed layer is covered with photoresist, which is cleared only in the locations where contacts are desired. There, electroplating will produce a metal film, forming soldering points for the device to the target substrate that will form its base. In this case, copper is used as the plating material, thanks to its high conductivity and solderability. The device is released from the mold by ion milling away the thin seed layer, then dissolving the oxide lining with a hydrofluoric (HF) acid wet etch. The free standing portion of the microactuator is thus ready for bonding to the target. The mold, meanwhile, may be used again after a simple cleaning step.

The target substrate may be prepared in several ways. The target shown above consists simply of indium solder bumps and interconnects on a patterned seed layer, and is known as a "plating bus" arrangement. The seed layer is used for the same reasons as on the hexSil structure, but in this case the seed layer is patterned immediately, with the unwanted portions removed by sputter etching. This provides isolation where desired without having to etch the seed layer after the indium is in place. Photoresist is spun again, and patterned to uncover the remaining seed layer. A layer of indium is then electroplated everywhere that the seed layer is visible. Indium acts as the solder when the two parts of the microactuator are pressed together, forming a cold weld to the copper at 200-300 MPa that was found suitable for hard disk requirements, as shown in figure 11h.

3.3 Electrostatic microactuator example two

3.3.1 Basic process: Silicon-on-insulator

The high-aspect ratio microactuator described in this section is in development at the University of California, Berkeley, and demonstrates another way to create the features required of an actuated slider. The microactuator is translational, with parallel-plates actuation and includes two of the design options described previously: integrated isolation plugs, as described in section 2.3.2, and a capacitive sensing array, as described in section 2.4.1. A picture of the basic design is shown in Fig. ??; a central shuttle holding the slider is supported by four folded-flexure springs and driven by parallel-plates arrays. Successful processing of the design is centered around the ability to etch very straight, narrow trenches using deep reactive ion etching (DRIE). Deep reactive ion-etching is a special plasma etching sequence that uses polymerization of the sidewalls of a trench to keep the walls straight even at extreme aspect ratios. Deep, narrow trenches make possible a microactuator with both closely packed electrostatic arrays and good mechanical strength. Conventional surface micromachining is used to produce the majority of the electrical interconnects.

[Figure 12 about here.]

[Figure 13 about here.]

The basic fabrication process uses a silicon-on-insulator (SOI) wafer to control DRIE trench depth. SOI wafers are very useful in microfabrication as they provide a layer of single-crystal silicon (the device layer) that is separated from the bulk of the wafer (the handle layer) by a thin layer of buried silicon oxide. This gives a very well controlled thickness to finished device, but is very expensive. The microactuators described here are fabricated from an SOI wafer with a 100 μm device layer. A variation on the processing sequence and layout eliminates the need for SOI wafers, and will be discussed in the following section.

The first stage of fabrication is creation of deep isolation trenches (see figure 13a-c). This procedure has been adapted to MEMS from integrated circuit processing for isolating thick MEMS structures (Brosnihan *et al.*, 1997). The isolation pattern is formed by photolithography and etched by DRIE down to the buried oxide. With trenches only 2 μm wide, this corresponds to an aspect ratio of 50:1. The wafer surface and trenches are then coated with LPCVD silicon nitride, which acts as the electrical insulator. The trench is then refilled in its entirety with LPCVD polysilicon, which is a more conformal material and better fills the trench than silicon nitride would alone; polysilicon also has much lower residual stresses than silicon nitride. The refill leaves a layer of polysilicon on the surface of the substrate, which must be etched or polished back to the silicon nitride. After etch-back, a second layer of LPCVD nitride completes isolation between regions.

Next, electrical interconnects are formed, as shown in figure 13d-f. Contact holes to the substrate are defined by photolithography, and etched by reactive ion etching of the silicon nitride. Metal lines may then be patterned directly by photolithography, or formed by lift-off. In a lift-off process, photoresist is deposited and patterned before the metal. The metal is then deposited vertically, so that the sidewalls of the resist are uncovered. Dissolving the resist allows the metal on top to float away, leaving

behind the interconnect pattern. In the figures shown here, the interconnects are formed by evaporated aluminum, eliminating the need for electroplating and a seed layer. The ability to isolate portions of the substrate is useful for simplifying the interconnect layout, as one interconnect can cross another by passing underneath it through an isolated portion of the substrate.

Finally, structural lithography is performed and a second etch by DRIE is done, as shown in figure 13g. These trenches will define the shape of the microactuator, and are larger, $4\ \mu\text{m}$ wide, to allow sufficient rotor travel. After this etch step, the device layer on the SOI buried oxide consists of fully defined into microactuators. When the buried oxide is removed by wet etching, the microactuator is released from the substrate (figure 13h) and, after removal of the photoresist that protected the device surface from HF during release, ready for operation. Thanks to the high aspect ratios of DRIE and the efficient integrated isolation scheme, the microactuator can theoretically be operated with a DC bias voltage of 15 Volts on the rotor, and a dynamic stator voltages below 5 Volts. In practice, higher voltages are required due to spreading of the trench walls over the course of DRIE. A picture of the electrostatic structure, with the rotor fingers on the left and the stator fingers on the right, divided down the center by isolation trenches, is shown in figure 14.

[Figure 14 about here.]

3.3.2 Variation: Anisotropic backside release

[Figure 15 about here.]

An alternative fabrication approach is to build the microactuator from a pure silicon wafer, but then, since the microactuator shouldn't be more than $100\ \mu\text{m}$ thick to fit in a HDD, etch away the backside of the wafer to obtain devices of that size. The main reason for using a silicon-only wafer is to reduce the need for expensive SOI wafers, which cost approximately 10 times as much as single-material wafers. Another benefit is elimination of the need for etch holes to reach the buried oxide layer, which increase vulnerability of microactuators to particle or moisture contamination. However, the thickness of the devices cannot be controlled as accurately as with the SOI process, and the processing sequence is more complicated.

Control of backside etching is difficult, making it hard to obtain devices with uniform thickness across a wafer. A proposed solution is to use an anisotropic wet etchant during the backside etch step. Anisotropic etchants etch very slowly on certain crystal planes of a single-crystal silicon wafer; a coating on trench sidewalls can protect fast-etching planes when the etchant reaches the trenches from the back, causing slow-etching crystal planes to begin coming together slowing the etch. The result is a nearly self-stopping etch with a V-shaped profile that prevents overetching even in the presence of nonuniformities in etch rate and trench depth across the wafer. The most common anisotropic etchants are potassium hydroxide (KOH), and tetramethyl ammonium hydroxide (TMAH). This release process is referred to here as an anisotropic backside release (ABR).

The key to a good release by this method is to achieve excellent protection of the top of the wafer and the deep trenches from the etchant, and this necessitates changes in the process flow from that for an SOI wafer. Without a good protective film, the interconnects on the surface of the wafer could be destroyed, or the fast-etching planes might be attacked along the trench

sidewalls. Of the etchants mentioned above, TMAH is preferred, due to high selectivity to both silicon oxide and nitride, and especially thermally grown oxide, which can be used as protective films. However, growing thermal oxide and/or depositing high-quality nitride are high temperature processes not compatible with most metals, so the structural trenches must be etched and oxidized before forming the electrical interconnects. As shown in figure 15c-d, the isolation trenches are formed as before, but the structural trenches are patterned and etched in the very next step. A thermal oxide is then grown in the trenches to produce the protective oxide layer (figure 15e).

To do lithography for the interconnects at this point, then, the surface of the wafer must be planarized. This is done by refilling the trenches with spin-on-glass. The spin-on-glass plugs the trenches nearly to the top, and can be sacrificed along with the thermal oxide at the end of the process. Extra glass on the wafer surface can be removed by a quick HF dip or chemical mechanical polishing. The resulting surface is uneven, as shown in figure 15f, but a thick photoresist layer can be applied over the trenches evenly enough to accomplish contact and metal patterning lithographies. After metallization much the same as for the soi wafer (figure 15g), a final coating of etch resistant material is required to protect the metal during backside release, as shown in figures 15h-j. After ABR, the backside of the device will be shaped by crystal planes, but the thickness of the device at the edge of DRIE features will be fixed. While a combination of silicon oxide and silicon nitride has been effective over a “metallization” of undoped polysilicon, an effective combination of true metal interconnects and protective films has yet to be found and is an ongoing area of research for improving the ABR process sequence.

A prototype microactuator with integrated gimbal fabricated using ABR is shown in figure 16. This prototype was operated with a 30 V DC bias and +/- 8 V AC driving voltage for +/- 1 μm displacement, while a larger version (shown in figure ??) was operated at 15 V bias and +/- 3 V driving. This layout and fabrication concept is currently being adjusted to fit a MEMS-ready suspension for more advanced testing.

[Figure 16 about here.]

3.4 Other fabrication processes

3.4.1 IBM electroplated microactuator

Where the DRIE-based process described above “digs” the microactuator out of a wafer, a procedure developed by IBM “grows” a microactuator with high-aspect ratio trenches on top of a wafer (Hirano *et al.*, 1999b). This is done by a clever sequence of electroplating steps and sacrificial depositions. First, an oxide sacrificial film is patterned, then covered with a metal seed layer. When later removed, the sacrificial will have left a gap between the microactuator and substrate portions of the microactuator needed to move freely. A polymer, 40 μm thick, is spun onto the wafer and patterned with a reverse image of the main structural layer. Trenches are etched down to the sacrificial layer by plasma etching, then refilled via electroplating, much like micro-molding. Another sacrificial polymer, photoresist this time, separates the top of the fixed portions of the structure from the platform upon which the slider will sit, while conveniently planarizing the surface for further lithography. The platform is created by two more electroplating steps on top of the parts of the structure that will move freely. Removal of the sacrificial layers (photoresist, polymer, and oxide) releases the microactuator for use.

This process has been used to produce both rotary and linear microactuators, and is comparatively advanced from a commercial standpoint. The resulting devices are thinner than those described in the previous example, but a similar aspect ratio (20:1) can be achieved. This procedure also has the benefits of being a low temperature process, which helps decrease processing cost and is compatible with the thin film magnetic head manufacturing process. Moreover, it includes an upper structure that covers the fingers, which improves device reliability by shielding the fingers from particles.

Additional fabrication details and dynamic testing results for the IBM design may be found in references (Hirano *et al.*, 1999b) and (Hirano *et al.*, 1999a). Certain control results are described in section 4.2.1

3.4.2 Electroplated microactuators with fine gaps

Finally, fabrication processes developed at the university of Tokyo demonstrate additional techniques for obtaining very small gaps between electrostatic fingers (Iizuka *et al.*, 2000). Similarly to the IBM process, electrostatic fingers are electroplated, in this case by nickel, within a polymer pattern. The gap between closely spaced fingers, however, is then formed by a sacrificial metal. Photoresist is used to cover the fingers except for the surfaces where a small gap is desired, which are electroplated with sacrificial copper, making possible narrow, well-defined gaps, perhaps most reliably of the processes described here. Continuing with a second nickel electroplating step creates the interlaced fingers, which will also support the slider; the wafer is polished down to level the structure. Finally, the copper, photoresist, and seed layer are etched away, leaving the free standing structure.

In another version of process, photoresist alone separates the stator and rotor fingers. In this case, a thin layer of photoresist is left where small gaps are desired, instead of growing a layer of copper. This method is dependent on excellent alignment, but can eliminate the need for polishing after the second electroplating step.

3.5 Suspension-level fabrication processes

3.5.1 PZT actuated suspensions

The long, highly integrated fabrication processes required by actuated slider microactuators contrast greatly with the fabrication of actuated suspension microactuators. In most cases, actuated suspensions use piezoelectric (PZT) drivers that are cut or etched as single, homogeneous pieces and attached to the steel suspension. Nevertheless, microfabrication techniques can still be useful in suspension processing. For example, some recent suspensions have used thin film PZT deposited on a substrate by sputtering for incorporation in a suspension. This is intended to produce a higher quality PZT films, and begins to introduce MEMS-style processing techniques even into suspension-scale manufacturing (Kuwayama and Matsuoka, 2002), (Lou *et al.*, 2002).

3.5.2 Integrated silicon suspension

Another area where silicon processing has been suggested for use on a suspension is the gimbal region, or even the entire suspension, as described in (Chen, 2001). An integrated silicon suspension would incorporate aspects of both actuated suspension and actuated slider fabrication. Force is provided by four piezes of bulk PZT cut down to size, as in other actuated suspensions, but the rest of the suspension is fabricated from single-crystal silicon by bulk micromachining.

The fabrication process for the integrated suspension is the precursor to the ABR process used to fabricate the microactuator in 3.3.2. Layers of LPCVD silicon nitride and polysilicon are deposited on a bare silicon wafers. The polysilicon is doped by ion implantation and covered with a second layer of nitride. The outline of the suspension and any spaces within it are then lithographically patterned. After a reactive-ion nitride etch to reach the substrate, trenches are etched by DRIE. The trenches are then plugged with spin-on-polymer for further lithography. First, the top layer of polysilicon is patterned into piezoresistive strips for sensing vibration. Second, a layer of photoresist is patterned for copper lift-off, to create metal interconnects. Finally, the planarizing polymer is removed and the entire surface is coated with silicon nitride. This final coating protects the top surface during an anisotropic backside wet etch, in this case by potassium hydroxide.

3.5.3 Instrumented suspensions

Finally, microfabrication techniques may be useful for installing sensors on conventional steel suspensions. The concept is to deposit a dielectric and a piezoresistive material on the stainless steel sheet that will be formed into the central piece of the suspension, and pattern piezoresistors directly by lithography and plasma etching. A second lithography may be used to add metal lines back to the e-block. Vibration sensors on the suspension are very desirable for controlling slider position, and the use of thin-film deposition and photolithography permits the sensors to be located at the points most effective for detecting vibration. An example of a sensor formed by this method is shown in figure 17

[Figure 17 about here.]

3.6 Actuated head fabrication

Several interesting fabrication processes have been proposed for another approach to creating a dual-stage disk drive servo: the actuated head. In an actuated head, the actuator is built into the slider, and moves just the read-write head. This could potentially eliminate many of the mechanical limits of actuated suspensions or actuated sliders. Actuation techniques are typically similar to those of actuated sliders, with the key complication being the need to integrate an actuator fabrication process with a slider fabrication process. Ways in which this might be done are discussed below.

One fabrication approach to actuating a read/write head is to enclose an electrostatic driving array inside a slider. The slider is built up from on a glass or Si substrate, beginning with the air-bearing surface (ABS), followed by a microactuator, and then surrounded by the remainder of the slider. The ABS is formed by silicon oxide deposited over aluminum and tapered photoresist

layers that give it a contoured shape. The majority of the ABS is then covered with photoresist, while a block in the center is plated with nickel and etched to form the electrostatic actuator. This, in turn, is covered while the remainder of the slider body is electroplated. The slider may then be bonded to a suspension and the ABS surface released from the substrate by etching away the original aluminum and photoresist surface (Imamura *et al.*, 1998).

The sacrificial metal technique described in section 3.4.2 is another possibility for building an electrostatic array onto a slider. It can be used to form small array with very narrow gaps, and the process is compatible with slider and head materials (Fujita *et al.*, 1999).

A third actuated head process makes use of an SOI wafer and silicon based materials. For this structures, a 20 μm device layer is coated with silicon nitride. The nitride is patterned with contact holes for connections to the substrate and used as insulation over the rest of the device. A layer of molybdenum is sputter deposited to perform interconnections to both the head and the electrostatic array. This array is formed by DRIE to the buried oxide, using a lithographically patterned hard mask of tetraethylorthosilicate. The result is simple, tiny, actuator that must be bonded to the edge of a slider after release from the SOI wafer (Kim and Chun, 2001).

4 Servo Control Design of MEMS Microactuator Dual-Stage Servo Systems

4.1 Introduction to disk drive servo control

The objective of disk drive servo control is to move the head to the desired track as quickly as possible, which is referred to as track seek control, and once on-track, position the head on the center of the track as precisely as possible, which is referred to as track-following control, such that data can be read/written quickly and reliably. The implementation of the servo controller relies on the position error signal (PES), which is obtained by reading the position information encoded on the disk's data tracks.

The position error is also called track mis-registration (TMR) in the disk drive industry. Major TMR sources in the track-following mode include spindle runout, disk fluttering, bias force, external vibration/shock disturbance, arm and suspension vibrations due to air turbulence, PES noise, written-in repeatable runout, residual vibration due to seek/settling, etc. (Ehrlich and Curran, 1999). These sources can be categorized as runout, r , input disturbance, d , and measurement noise, n , by the locations they are injected into the control system, as shown in Fig. 18. In Fig. 18, $G_P(s)$ and $G_C(s)$ are the disk drive actuator and the controller; r and x_p represent track runout and head position respectively.

[Figure 18 about here.]

From Fig. 18, the *PES* can be written as

$$PES = S(s)r + S(s)G_P(s)d - S(s)n. \quad (9)$$

Thus, the TMR rejection can be represented by the closed loop sensitivity function $S(s)$, which is defined by

$$S(s) = \frac{1}{1 + G_C(s)G_P(s)}. \quad (10)$$

The higher the bandwidth of the control system, the higher the attenuation of the sensitivity function $S(s)$ below the bandwidth. Thus, one of the most effective methods to reduce PES and increase servo precision is to increase the control system bandwidth.

Traditional disk drive servo systems utilize a single voice coil motor, or VCM, to move the head. Multiple structure resonance modes of the E-block arm and the suspension located between the pivot and the head impose a major limitation on the achievable control bandwidth. A dual-stage servo system using a MEMS actuated-slider microactuator can achieve high bandwidth because the microactuator is located between the suspension and the slider, thus by-passing the pivot, E-block arm and the suspension resonance modes.

One basic task of dual-stage servo control design is to increase control bandwidth using the second stage actuator. Many design methodologies have been developed to accomplish this objective. In this section, major dual-stage servo control design methodologies are first reviewed, and design considerations for controller design of a MEMS dual-stage servo system are discussed. As design examples, the details of track-following control designs using a sensitivity function decoupling design method and the μ -synthesis design method are presented in subsection 4.3. In subsection 4.4, a short-span seeking control scheme using dual-stage actuator based on a decoupled feed forward reference trajectory generation is introduced .

4.2 Overview of dual-stage servo control design Methodologies

Various control design architectures and methodologies have been developed for dual-stage servo control design. They can be largely classified into two categories: those based on decoupled or sequential single-input-single-output (SISO) designs, and those based on modern optimal design methodologies, such as LQG, LQG/LTR, H_∞ , and μ -synthesis, in which the dual-stage controllers are obtained simultaneously.

Two constraints must be considered in dual-stage servo control design. First, the contribution from each actuator must be properly allocated. Usually, the first stage actuator, or the coarse actuator, has a large moving range, but a low bandwidth, while the second stage actuator, or the fine actuator, has a high bandwidth, but small moving range. Second, any destructive effect, in which the two actuators fight each other by moving in opposite directions, must be avoided.

4.2.1 Classical SISO design methodologies

Several architectures and design methodologies have been proposed to transform the dual-stage control design problem into decoupled or sequential multiple SISO compensators design problems, for example, master-slave design, decoupled design (Mori *et al.*, 1991), PQ method (Schroeck *et al.*, 2001), and direct parallel design (Semba *et al.*, 1999). Fig. 19 to Fig. 22 shows the block diagrams of dual-stage controller design using these methods. In these figures, G_1 and G_2 represent the course actuator (VCM) and fine actuator (microactuator) respectively; x_1 is the position of the course actuator; x_r is the position of the fine actuator relative to the course actuator; x_p is the total position output; r is the reference input (runout), and PES is the position error, $e = r - x_p$.

Master-slave design: In a traditional master-slave structure, the absolute position error is fed to the fine actuator, and output of the fine actuator is fed to the coarse actuator, as shown in Fig. 19. The position error will be compensated by the high bandwidth

fine actuator. The coarse actuator will follow the fine actuator to prevent its saturation.

[Figure 19 about here.]

Decoupled design: Fig. 20 shows the decoupled design structure (Mori *et al.*, 1991), which is similar to the master-slave structure. However, instead of feeding just the fine actuator output to the coarse actuator, the summation of the fine actuator output and the position error is fed, which equals the position error of the coarse actuator. A very nice feature of this structure is that the control system is decoupled into two independent control loops, and the total sensitivity function is the product of the sensitivity functions of each of the control loops (Li and Horowitz, 2001). Thus, the two compensators C_1 and C_2 can be designed independently. Decoupled design is also called decoupled master-slave design, or sensitivity function decoupling design. In section 4.3.2, details of a track-following controller designed using this method will be further discussed.

[Figure 20 about here.]

Both the master-slave and the decoupled designs use the relative position of the fine actuator, x_r . If a relative position sensor is unavailable, x_r can be estimated using a model of the fine actuator.

PQ design method: The PQ method is another innovative design technique for control design of dual-input, single-output system (Schroeck *et al.*, 2001). A block diagram of a dual-stage control design using this method is shown in Fig. 21.

[Figure 21 about here.]

In PQ design, P is defined by

$$P = \frac{G_1}{G_2}, \quad (11)$$

and a dual-stage controller can be designed in two steps. The first involves the design of an auxiliary compensator Q for plant P , which is defined by

$$Q = \frac{C_1}{C_2}. \quad (12)$$

Q is designed to parameterize the relative contribution of the coarse and fine actuator. The 0dB crossover frequency and phase margin of the open loop transfer function PQ are the design parameters in the design of Q . At frequencies below the 0dB crossover frequency of PQ , the output is dominated by the coarse actuator, while at frequencies above the 0dB crossover frequency, the output is dominated by the fine actuator. At the 0dB crossover frequency, the contribution from the two actuators are equal. A large phase margin of PQ will ensure that the two actuators will not fight each other when their outputs are close in magnitude, thus avoiding any destructive effects can be avoided.

The second step in the PQ design methodology is to design a compensator C_0 for SISO plant PQ that satisfies the bandwidth (crossover frequency), gain margin, phase margin, and error rejection requirements of the overall control system.

Direct parallel design: It is also possible to design the dual-stage controller directly using a parallel structure, as shown in Fig. 22, by imposing some design constraints and sequential loop closing (Semba *et al.*, 1999).

[Figure 22 about here.]

The two constraints for parallel design in terms of the *PES* open loop transfer functions are (Semba *et al.*, 1999):

$$C_1(s)G_1(s) + C_2(s)G_2(s) \rightarrow C_2(s)G_2(s), \quad (13)$$

at high frequencies and

$$|C_1(s)G_1(s) + C_2(s)G_2(s)| \gg |C_1(s)G_1(s)|, \quad (14)$$

at low frequencies. The first constraint implies that open loop frequency response of the dual-stage control system at high frequencies approximately equals that of the fine actuator control loop. Thus, the compensator $C_2(s)$ can be first designed independently as a SISO design problem to satisfy the bandwidth, gain margin, and phase margin requirements of the dual-stage control system. Compensator $C_1(s)$ can then be designed for the SISO plant model with the fine actuator control loop closed. This model is defined by:

$$G(s) = \frac{G_1(s)}{1 + C_2(s)G_2(s)}, \quad (15)$$

such that the low frequency constraint and overall stability requirement are satisfied.

A dual-stage controller for a MEMS dual-stage actuator servo system has been designed using this method and implemented at IBM. An open loop gain crossover frequency of 2.39 kHz with gain margin 5.6 dB and phase margin 33° was obtained. In experimental testing, a $1 - \sigma$ TMR of 0.024 μm has been achieved (Semba *et al.*, 1999).

4.2.2 Modern MIMO design methodologies

Since the dual-stage actuator servo system is a MIMO system, it is natural to utilize modern MIMO optimal design methodologies, such as LQG, LQG/LTR, H_∞ , and μ -synthesis, to design the dual-stage controller. Usually MIMO optimal designs are based on the parallel structure shown in Fig. 22, augmented with noise/disturbances models and other weighting functions to specify the control design performance objectives.

Linear quadratic Gaussian (LQG) control combines a Kalman filter and optimal state feedback control based on the separation principle. However, the Kalman filter weakens the desirable robustness properties of the optimal state feedback control. Linear quadratic Gaussian / loop-transfer recovery (LQG/LTR) control recovers robustness by a Kalman filter redesign process. Dual-stage control designs using LQG and LQG/LTR have been reported in (Suzuki *et al.*, 1997), (Hu *et al.*, 1999), (Suh *et al.*, 2002), etc.

The LQG design methodology minimizes the H_2 norm of the control system, while H_∞ design methodology minimizes the H_∞ norm of the control system. μ -synthesis design methodology is based on H_∞ design and accounts for plant model uncertainties during the controller synthesis process with guaranteed robustness. Dual-stage control designs based on H_∞ and μ -synthesis design methodologies have been reported in (Suzuki *et al.*, 1997), (Hernandez *et al.*, 1999), (Rotunno and de Callafon, 2000), etc. Some details of a control design using μ -synthesis for the MEMS actuator dual-stage servo system will be presented in section 4.3.3

Other advanced control theories also have been applied to dual-stage servo control designs, such as sliding mode control (Lee *et al.*, 2000) and neural networks (Sasaki *et al.*, 1998).

4.3 Track-Following Controller Design for a MEMS microactuator dual-stage servo system

4.3.1 Servo design considerations for MEMS microactuators

MEMS microactuators, or MAs, for dual-stage servo application are usually designed to have a single flexure resonance mode between 1-2 kHz (Horsley *et al.*, 1999), (Fan *et al.*, 1999). This resonance mode is usually very lightly damped and can have a $\pm 15\%$ variation due to variations in the fabrication process. Since the uncertain resonance frequency is relatively low and close to the open loop gain crossover frequency of the servo system, controller robustness to these variations must be considered in the controller design.

Capacitive sensing can be utilized in MEMS microactuators to measure the position of the microactuator relative to the VCM actuator (Horsley *et al.*, 1999), (Wongkomet, 1998). However, this requires additional sensing electronics and wires to and from the head gimbal assembly (HGA), which result in additional fabrication and assembly costs. Thus, whether or not a relative position sensor will be used in MEMS dual-stage servo systems is still an open question. If the MA's resonance mode is lightly damped, it is susceptible to airflow turbulence and external disturbances. The relative position signal can be utilized to damp the MA's resonance mode. Dual-stage control can be classified as MIMO or SIMO designs according to the availability of the relative position signal.

Given the fact that the inertia of the MEMS MA is very small compared to that of the VCM, the effect of the motion of the MA on the VCM can be neglected. By feeding the control input of the VCM to the input of the MA with a proper gain, we can cancel the coupling effect of the VCM on the MA (Li and Horowitz, 2001). Thus, the dual-stage control model can be decoupled as the sum of the outputs of the VCM and the MA, as shown in Fig. 23, in which G_V , G_M are the VCM and MA models respectively, and x_p is the absolute position of the read/write head, which equals the absolute position of the VCM, x_v , and the position of the MA relative to the VCM, $RPES$.

[Figure 23 about here.]

4.3.2 Decoupled track-following control design and self-tuning control

Sensitivity function decoupling design methodology: Fig. 24 shows a block diagram used for decoupled control design of the MEMS MA dual-stage servo systems (Li and Horowitz, 2001). The part enclosed in the dashed box on the upper-right corner is the dual-stage plant model shown in Fig. 23. In the figure, G_V and G_M are the VCM and MA models respectively; x_p is the absolute position of the read/write head; x_v is the absolute position of the VCM actuator; and $RPES$ is the position of the MA relative to the VCM; r represents the track runout, and PES is the position error signal of the head relative to the data track center.

[Figure 24 about here.]

The decoupling control approach, originally introduced in (Mori *et al.*, 1991), utilizes the PES and $RPES$ signals to generate the position error of the VCM relative to the data track center, which will be labeled as $VPES$,

$$VPES = PES + RPES = r - x_v, \quad (16)$$

and this signal is fed to the VCM loop compensator.

As shown in the block diagram, there are three compensators that need to be designed: the VCM loop compensator K_V ; the MA *PES* loop compensator K_M ; and the MA *RPES* minor loop compensator $K_{MM} = K_{RR}/K_{RS}$, which is used to damp the MA's flexure resonance mode and place the closed loop poles of the MA *RPES* loop at an appropriate location. The damped MA closed loop transfer function G_R , shown in the lower-middle dashed box, is defined by

$$G_R = \frac{G_M}{K_{RS} + G_M K_{RR}}, \quad (17)$$

while the total dual-stage open loop transfer function from r to x_P , G_T , is

$$G_T = K_V G_V + K_M G_R + K_M G_R K_V G_V. \quad (18)$$

It can be shown that the block diagram in Fig. 24 is equivalent to the sensitivity block diagram shown in Fig. 25, and the total closed loop sensitivity function from r to *PES* equals the product of the VCM and microactuator loop sensitivities, S_V and S_M , respectively:

$$S_T = \frac{1}{1 + G_T} = S_V S_M, \quad (19)$$

where

$$S_V = \frac{1}{1 + K_V G_V}, S_M = \frac{1}{1 + K_M G_R}. \quad (20)$$

Thus, the dual-stage servo control design can be decoupled into two independent designs: the VCM loop and the microactuator loop design. The VCM loop sensitivity can be designed using traditional single-stage servo design methodologies. The microactuator loop sensitivity is designed to expand the bandwidth and increase the attenuation of low frequency runout and disturbances.

[Figure 25 about here.]

Closed loop sensitivity design by pole placement: For a typical sampled 2nd order system with the discrete time transfer function

$$G(q^{-1}) = \frac{q^{-1} B_o(q^{-1})}{A_o(q^{-1})}, \quad (21)$$

where q^{-1} is one step delay operator; $B_o(q^{-1})$ is the plant zero polynomial, and $A_o(q^{-1}) = 1 + a_1 q^{-1} + a_2 q^{-2}$ is the plant pole polynomial. The closed loop sensitivity function can be designed by pole placement, solving the following Diophantine equation (Åström and Wittenmark, 1995):

$$A_c(q^{-1}) = A_o(q^{-1})S(q^{-1}) + q^{-1}B_o(q^{-1})R(q^{-1}), \quad (22)$$

where $A_c(q^{-1})$ is the desired closed loop characteristic polynomial. The closed loop sensitivity function, G_S , is

$$G_S(q^{-1}) = \frac{A_o(q^{-1})S(q^{-1})}{A_c(q^{-1})}, \quad (23)$$

and the discrete time controller $C(q^{-1})$ is

$$C(q^{-1}) = \frac{R(q^{-1})}{S(q^{-1})}. \quad (24)$$

$A_c(q^{-1})$ can be chosen such that the required bandwidth and system response are satisfied. Usually it is more intuitive to describe it with its continuous time equivalent parameters: the damping ratio, ζ , and the natural frequency ω_n . The damping

ratio is directly related to the phase margin of the open loop transfer function. For a typical design, it can be chosen to be equal to or greater than 1, in order to ensure enough phase margin. ω_n is related to the control system's bandwidth, which is limited by sampling frequency and time delay, or the high frequency structural dynamics of the system.

Dual-stage Sensitivity Function Design: The compensators in the dual-stage servo system depicted in Fig. 24 can be designed by a two-step design process, as illustrated in Fig. 26

[Figure 26 about here.]

First, the VCM loop compensator K_V is designed to attain a desired VCM closed loop sensitivity S_V , as shown in the top part of Fig. 26. Its bandwidth, ω_{VC} in Fig. 26, is generally limited by the E-block and suspension resonance modes. The design of this compensator can be accomplished using conventional SISO frequency shaping techniques.

The second step of the design process involves the design of the MA loop compensators to attain additional attenuation S_M , as shown in the middle part of Fig. 26. This step is itself accomplished in two steps. First, the minor *RPES* loop compensator, K_{RR}/K_{RS} , is determined in order to damp the MA resonance mode and place the poles of G_R , or equivalently ω_{MR} in Fig. 26, at a desired location. The compensator can be obtained by solving a Diophantine equation by pole placement as discussed in the previous subsection. The poles of G_R will become the zeros of S_M .

Finally, the *PES* loop compensator K_M is designed to place the poles, or equivalently ω_{MC} in Fig. 26, of the MA loop closed loop sensitivity S_M . ω_{MC} is limited by the *PES* sampling frequency and computational time delay (Whilte and Lu, 1999).

The total dual-stage sensitivity is shown in the bottom part of Fig. 26. For a given ω_{MC} , the additional attenuation A_S , provided by the MA loop, will be determined by ω_{MR} . In our proposed procedure, the initial value of ω_{MR} can be chosen to be the same as ω_{VC} . It is then adjusted so that the desired attenuation and phase margin requirements of the overall dual-stage system are satisfied. Decreasing ω_{MR} increases the low frequency attenuation of the closed loop sensitivity function S_T , but also generally reduces the phase margin of open loop transfer function G_T .

For SIMO design when the *RPES* is not available, the MA model can be used as an open loop observer to estimate the *RPES*. The combination of the open loop observer and the minor loop compensator is equivalent to a notch filter.

Self-tuning control to compensate variations in the MA's resonance mode:

An adaptive control scheme can be combined with the decoupled discrete time pole placement design described above, to compensate variations in the MA's resonance mode, by tuning the MA *RPES* inner loop compensator.

A block diagram for the MA inner loop self-tuning control is shown in Fig. 27. The parameter adaptation algorithm (PAA) is a direct self-tuning algorithm, based on the MA inner loop pole placement design.

[Figure 27 about here.]

Consider the MA open loop transfer function in Eq. 21. Since the MA's resonance mode is lightly damped, the zero of the MA's discrete time transfer function is very close to 1 ($z_o \approx 1$). Thus, it is possible to factor out the "known" term $(1 + z_o q^{-1})$ from the Diophantine equation (22). The resulting *RPES* minor-loop closed loop dynamics is given by

$$A_c(q^{-1})y(k) = q^{-1}b_0(1 + z_o q^{-1})[K_{RS}(q^{-1})u_{MR}(k) + K_{RR}(q^{-1})y(k)],$$

where u_{MR} is the control input to the MA; y denotes the position of the MA relative to the VCM, i.e. $y = RPES$. Defining:

$$S(q^{-1}) = b_0 K_{RS}(q^{-1}) = s_0 + s_1 q^{-1}, \quad (25)$$

$$R(q^{-1}) = b_0 K_{RR}(q^{-1}) = r_0 + r_1 q^{-1}, \quad (26)$$

the regressor vector, $\phi(k)$ and filtered regressor vector, $\phi_f(k)$,

$$\phi(k) = [u_{MR}(k) \ u_{MR}(k-1) \ y(k) \ y(k-1)], \quad (27)$$

$$A_c(q^{-1})\phi_f(k) = (1 + z_o q^{-1})\phi(k), \quad (28)$$

and the controller parameter vector $\theta = [s_0 \ s_1 \ r_0 \ r_1]^T$, the closed loop $RPES$ dynamics (25) can be rewritten as

$$y(k) = \theta^T \phi_f(k-1). \quad (29)$$

From Eq. (29), the controller parameter vector estimate $\hat{\theta}(k) = [\hat{s}_0(k) \ \hat{s}_1(k) \ \hat{r}_0(k) \ \hat{r}_1(k)]^T$ can be updated using a standard recursive least square algorithm (RLS) (Åström and Wittenmark, 1995):

$$\hat{\theta}(k) = \hat{\theta}(k-1) + P(k)\phi_f(k)e^o(k), \quad (30)$$

$$e^o(k) = y(k) - \hat{\theta}^T(k-1)\phi_f(k-1), \quad (31)$$

$$P(k) = \left[P(k-1) - \frac{P(k-1)\phi_f(k-1)\phi_f^T(k-1)P(k-1)}{1 + \phi_f^T(k-1)P(k-1)\phi_f(k-1)} \right], \quad (32)$$

The control law is

$$\hat{S}(k, q^{-1})u_{MR}(k) = \hat{S}_o(k)u_M(k) - \hat{R}(k, q^{-1})y(k), \quad (33)$$

with

$$\hat{S}(k, q^{-1}) = \hat{s}_0(k) + \hat{s}_1(k)q^{-1}, \quad (34)$$

$$\hat{R}(k, q^{-1}) = \hat{r}_0(k) + \hat{r}_1(k)q^{-1}, \quad (35)$$

and $u_{MR}(k)$ being the output of the MA fixed outer loop compensator K_M , $u_M(k)$ being the control input to the MA.

4.3.3 Dual-Stage Track-Following Control Design using μ -Synthesis

Design methodology: μ , the structured singular value, is a measure of how big a perturbation to a system needs to be to make the system unstable. By incorporating a fictitious uncertainty block, robust performance in terms of H_∞ norm of the closed loop transfer function can be related to the value of μ . μ -synthesis is a robust optimal controller design technique that attempts to minimize μ through an iterative process (Balas *et al.*, 1995).

For controller design using μ -synthesis, the model uncertainties are represented using linear fractional transformations (LFT). Disturbances and outputs are weighted to characterize the real plant environment and the performance requirements. A block diagram used for dual-stage μ -synthesis controller design is shown in Fig. 28.

[Figure 28 about here.]

In the block diagram, two model uncertainties, δ_1 and δ_2 , are considered. δ_1 is an additive uncertainty used to describe the VCM unmodeled dynamics. δ_2 represents the parametric uncertainty in the stiffness of the microactuator.

Disturbance signals accounted for in the model include the track runout r , input disturbances to the VCM and microactuator, d_{VCM} and d_{MA} , respectively, the PES sensor noise n_{PES} and the $RPES$ sensor noise n_{RPES} . These disturbance signals are generated by passing normalized signals \bar{r} , $\overline{d_{VCM}}$, $\overline{d_{MA}}$, $\overline{n_{PES}}$ and $\overline{n_{RPES}}$ through weights W_r , $W_{d_{VCM}}$, $W_{d_{MA}}$, $W_{n_{PES}}$ and $W_{n_{RPES}}$, respectively, which can be either constants or frequency shaping filters. These weights are selected by the designer so that disturbances are modeled with sufficient fidelity.

The output signals in the synthesis model are head position error signal, PES , the microactuator relative position signal, $RPES$, the VCM control input u_{VCM} , and the MA control input u_{MA} . These signals are multiplied by scaling factors, W_{PES} , W_{RPES} , $W_{u_{VCM}}$, and $W_{u_{MA}}$, respectively, to produce the weighted performance signals \overline{PES} , \overline{RPES} , $\overline{u_{VCM}}$, $\overline{u_{MA}}$. The scaling factors are selected to characterize the performance requirements.

Given a set of input and output weights and plant uncertainties, if the controller synthesized achieves

$$\mu \leq \beta, \quad (36)$$

the closed loop transfer function, \overline{T} , from the normalized disturbances

$$\overline{d} = [\overline{r} \ \overline{d_{VCM}} \ \overline{d_{MA}} \ \overline{n_{PES}} \ \overline{n_{RPES}}] \quad (37)$$

to the weighted performance signals

$$\overline{e} = [\overline{PES} \ \overline{RPES} \ \overline{u_{VCM}} \ \overline{u_{MA}}] \quad (38)$$

will have infinity norm

$$\|\overline{T}\|_{\infty} \leq \beta \quad (39)$$

for perturbations

$$\|\Delta\|_{\infty} = \left\| \begin{bmatrix} \delta_1 & 0 \\ 0 & \delta_2 \end{bmatrix} \right\|_{\infty} \leq \frac{1}{\beta}. \quad (40)$$

The interpretation of H_{∞} as the RMS gain of the sinusoid to help understand the design is as follows. Assume that each element \overline{d}_i of the disturbance input vector in Eq. (37) is a sinusoid of the form

$$\overline{d}_i(t) = D_i \sin(\omega_i t + \psi_i), \quad (41)$$

such that

$$\sum_{i=1}^5 D_i^2 \leq 1. \quad (42)$$

Then the steady state response of output in Eq. (38) will also be a sinusoid of the form

$$\overline{e}_i(t) = E_i \sin(\omega_i t + \phi_i), \quad (43)$$

and

$$\sum_{i=1}^4 E_i^2 \leq \beta, \quad (44)$$

under the perturbations in Eq. (40)

Weighting functions for μ -synthesis design:

Performance weights are chosen based on limits that the error signals should not exceed. The limit on the PES is based on a rule of thumb commonly used in the disk drive industry which states that the position error of the head should not exceed 1/10 of a track width during track following. $RPES$ is limited by the stroke limit of the MA. Thus,

$$W_{PES} = \frac{10}{\text{track width}}; W_{RPES} = \frac{1}{\text{stroke limit}}. \quad (45)$$

Weights on control inputs are based on the control input saturations.

$$W_{U_{VCM}} = \frac{1}{(i_V)_{max}}; W_{U_{MA}} = \frac{1}{(v_M)_{max}}, \quad (46)$$

where $(i_V)_{max}$ and $(v_M)_{max}$ are the maximum drive current of the VCM and the maximum drive voltage of the MA respectively.

The weights for PES noise, n_{PES} , and the disturbance to the VCM, w_{dVCM} , were determined by extrapolating the PES decomposition results presented in (Ehrlich and Curran, 1999). The weight of the $RPES$ sensing noise, n_{RPES} , is assumed to be 8 nm (Wongkomet, 1998). The disturbance weight, w_{dMA} is assumed to be 0.1V in the design.

The runout weighting is a low pass filter that captures the combined effects of track runout, mechanical vibrations, and bias force disturbance to PES ,

$$W_r = \frac{2 * 10^{-8}(s + 2\pi * 10)^2}{(s + 2\pi * 1000)^2}. \quad (47)$$

The combination of W_{PES} and W_r determines the closed loop sensitivity function from r to PES , $S(s)$, of the dual-stage system.

$$\| W_{PES}S(s)W_r \|_{\infty} \leq \beta. \quad (48)$$

If $\beta = 1$, the magnitude of bode plot of $S(s)$ lies below that of $\frac{1}{W_{PES}W_r}$.

For SIMO design, the controller to be synthesized has only one input. In the synthesis model, $RPES$ is not fed to the controller K , and $RPES$ noise n_{rpes} and its weights W_{nRPES} are not used.

4.3.4 Design and simulation results

Fig. 29 shows the Bode plots of the open loop transfer functions from r to x_p and the closed loop sensitivity functions of the two designs, respectively. Sampling frequency was chosen to be 20 kHz in both designs.

[Figure 29 about here.]

For the decoupled MIMO design, the gain crossover frequency, gain margin, phase margin of the open loop system are 2201 Hz, 9.1 dB, and 48.8°, respectively. For the decoupled SIMO design, they are 2381 Hz, 8.7 dB, and 30.6°, respectively.

For μ -synthesis MIMO design, the gain crossover frequency, gain margin, phase margin of the open loop system are 2050 Hz, 9.5 dB, 66.0°, respectively. For μ -synthesis SIMO design, they are 2223 Hz, 2.9 dB, 32.0°, respectively.

The controller design above has not been implemented on a MEMS microactuator dual-stage servo system. However, controllers designed using both methods have been tested on a PZT actuated suspension dual-stage servo system, validating their effectiveness (Li and Horowitz, 2002).

Fig. 30 shows the simulation of control parameters adaptation for the self-tuning controller, when the real microactuator resonance frequency is 1.2 times its nominal value. The controller parameters converged to their desired values. Similar responses were obtained when the real resonance frequency is 0.8 times the nominal value.

[Figure 30 about here.]

4.4 Dual-stage seek control design

Because the inertia of a microactuator is much smaller than that of the VCM, it can produce a larger acceleration and move faster than the VCM. However, the motion range of a microactuator is usually limited to a few micrometers. Thus, the performance improvement in seek control made possible by using dual-stage actuation will mainly be in short distance seeks.

Two degree-of-freedom (DOF) position control has been a very popular control technique in short distance seeks. A 2-DOF control technique utilizing decoupled feed forward reference trajectories has been developed for short span seek control using a PZT actuated suspension dual-stage servo system (Kobayashi and Horowitz, 2001). The same technique can also be applied to seek control of MEMS MA dual-stage servo system.

Fig. 31 shows a block diagram for dual-stage short span seek control design using this method. In the figure, x_V^d and x_R^d are the desired seek trajectories of the VCM and the MA respectively. K_{VF} and K_{RF} are Zero Phase Error Tracking Feedforward Controllers (ZPTFFC) generated with the VCM model G_V and the damped MA model G_R (Tomizuka, 1987).

[Figure 31 about here.]

To minimize the residual vibration after seek operation, minimum jerk seek trajectories were applied to both the VCM and the microactuator. These can be generated by (Mizoshita *et al.*, 1996)

$$x_V^d(t) = 60 d_s \left[\frac{1}{10} \left(\frac{t}{T_V} \right)^5 - \frac{1}{4} \left(\frac{t}{T_V} \right)^4 + \frac{1}{6} \left(\frac{t}{T_V} \right)^3 \right], \quad (49)$$

$$x_V^d = \begin{cases} 60 (d_s - x_V^d(T)) \left[\frac{1}{10} \left(\frac{t}{T} \right)^5 - \frac{1}{4} \left(\frac{t}{T} \right)^4 + \frac{1}{6} \left(\frac{t}{T} \right)^3 \right] & t \leq T \\ d_s - x_V^d(t) & t > T \end{cases}, \quad (50)$$

where d_s is the distance of the head from the target track; T is the time when the head reaches the target track if dual-stage actuator is used, while T_V is the time when the head reaches the target track if only VCM is used. T_V and T can be chosen based on the control force saturation and seek performance requirement.

Fig. 32 shows the $1\mu\text{m}$ seek response of the dual-stage actuator for the MIMO design. Overshoot was eliminated and there were no obvious residual vibrations. The seek time using the dual-stage actuator is about 0.25 ms, compared to a seek time of about 0.7 ms if only the VCM is used.

[Figure 32 about here.]

5 Conclusions

In order to increase hard disk drive storage density, high bandwidth dual-stage servo systems are necessary to suppress disturbances and increase servo precision. Various prototype MEMS microactuators have been designed and fabricated to provide a dual-stage actuation approach. The most common approach for these prototypes is to use electrostatic driving arrays produced by MEMS fabrication methods. Simulations and experiments show that integrated silicon gimbal designs and capacitive relative position sensing arrays can meet several important requirements for the use in HDDs. The use of structural electrical-isolation in the MA design could considerably reduce microactuator driving voltages, while processes that avoid the use of silicon-on-insulator wafers or high-temperature processing steps could reduce manufacturing costs. High bandwidth dual-stage track-following controllers have been designed using both a decoupled SISO design method, and robust μ -synthesis design methods, among others. Additionally, short-span seeking control using a 2-DOF control structure with decoupled feed forward trajectory generation can greatly reduce the short span seek time.

There remains much research needing to be done in this field to achieve nanometer-level precision. In order to further increase bandwidth, third generation dual-stage servo systems of an actuated head approach will eventually have to be employed. Research in this area has just started, with the key problem being how to combine microactuator fabrication with read/write head fabrication. Another area of research is to use MEMS technology to incorporate additional sensors to suppress the TMR due to airflow excited structural vibration. New robust, adaptive MIMO control architectures and algorithms must be developed for such a multi-sensing and multi-actuation servo system.

References

- Åström, K. J. and B. Wittenmark (1995). *Adaptive Control*. 2nd ed.. Addison-Wesley.
- Balas, G. J., J. C. Doyle, K. Glover, A. Packard and R. Smith (1995). *μ -Analysis and Synthesis ToolBox*. MUSYN Inc. and The MathWorks.
- Brosnihan, T.J., J.M. Bustillo, A.P. Pisano and R.T. Howe (1997). Embedded interconnect and electrical isolation for high-aspect-ratio, soi inertial instruments. In: *International Conference on Solid-State Sensors and Actuators*. New York, NY, USA. pp. 637–40.
- Chen, T.-L. (2001). *Ph.D. Dissertation: Design and Fabrication of PZT-Actuated Silicon Suspensions for Hard Disk Drives*. University of California. Berkeley, CA, USA.
- Chen, T., Y. Li, K. Oldham and R. Horowitz (2002). Mems application in computer disk drive drive dual-stage servo systems. *Journal of the Society of Instrumentation and Control Engineers* **41**, 412–20.
- Cheung, P., R. Horowitz and R. Howe (1996). Design, fabrication and control of an electrostatically driven polysilicon microactuator. *IEEE Transactionson Magnetics*.
- Ehrlich, R. and D. Curran (1999). Major hdd tmr sources, and projected scaling with tpi. *IEEE Transactionson Magnetics* **35**, 885–91.

- Fan, L.-S., T. Hirano, J. Hong, P. R. Webb, W.H. Juan, W. Y. Lee, S. Chan, T. Semba, W. Imano, T.S. Pan, S. Pattanaik, F.C. Lee, I. McFadyen, S. Arya, and R. Wood (1999). Electrostatic microactuator and design considerations for hdd application. *IEEE Transactions on Magnetics* **35**, 1000–5.
- Fujita, H., K. Suzuki, M. Ataka and S. Nakamura (1999). A microactuator for head positioning system of hard disk drives. *IEEE Transactions on Magnetics* **35**, 1006–10.
- Hac, A. and L. Liu (1993). Sensor and actuator location in motion control of flexible structures. *Journal of Sound and Vibration* **167**, 239–61.
- Hernandez, D., S.-S. Park, R. Horowitz and A.K. Packard (1999). Dual-stage track-following servo design for hard disk drives. In: *Proc. of American Automatic Control Conference*. pp. 4116–21.
- Hiramoto, K., H. Doki and G. Obinata (2000). Optimal sensor/actuator placement for active vibration control using explicit solution of algebraic riccati equation. *Journal of Sound and Vibration* **229**, 1057–75.
- Hirano, T., L.-S. Fan, T. Semba, W. Lee, J. Hong, S. Pattanaik, P. Webb, W.-H. Juan and S. Chan (1999a). High-bandwidth hdd tracking servo by a moving-slider micro-actuator. *IEEE Transactions on Magnetics* **35**, 3670–72.
- Hirano, T., L.-S. Fan, T. Semba, W.Y. Lee, J. Hong, S. Pattanaik, P. Webb, W.-H. Juan and S. Chan (1999b). Micro-actuator for tera-storage. In: *IEEE Int'l MEMS 1999 Conference*.
- Horsley, D. (1998). *Ph.D. Dissertation: Microfabricated electrostatic actuators for magnetic disk drives*. University of California, Berkeley, CA, USA.
- Horsley, D., N. Wongkomet, R. Horowitz and A. Pisano (1999). Precision positioning using a microfabricated electrostatic actuator. *IEEE Transactions on Magnetics* **35**, 993–99.
- Howell, T., R. Ehrlick and M. Lippman (1999). TPI growth is key to delaying superparamagnetism's arrival. *Data Storage* pp. 21–30.
- Hu, X., W. Guo and T. Huang and B.M. Chen (1999). Discrete time LQG/LTR dual-stage controller design and implementation for high track density HDDs. In: *Proc. of American Automatic Control Conference*. pp. 4111–15.
- I. Naniwa, S. Nakamura, S. Saegusa and K. Sato (1999). Low voltage driven piggy-back actuator of hard disk drives. In: *IEEE International MEMS 99 Conference*. Orlando, FL, USA. pp. 49–52.
- Iizuka, T., T. Oba and H. Fugita (2000). Electrostatic micro actuators with high-aspect-ratio driving gap for hard disk drive applications. In: *Int'l Symposium on micromechatronics and human science*. Nagoya, Japan. pp. 229–36.
- Imamura, T., M. Katayama, Y. Ikegawa, T. Ohwe, R. Koishi and T. Koshikawa (1998). Mems-based integrated head/actuator/slider for hard disk drives. *IEEE/ASME Transactions on Mechatronics* **3**, 166–74.
- Imamura, T., T. Koshikawa and M. Katayama (1996). Transverse mode electrostatic microactuator for mem-based hdd slider. In: *Proc. IEEE MEMS Workshop*. San Diego, CA, USA. pp. 216–21.

- Keller, C.G. and R.T. Howe (1997). Hexsil tweezers for teleoperated micro-assembly. In: *10th Int'l Workshop on Micro Electro Mechanical Systems (MEMS'97)*. Nagoya, Japan. pp. 72–77.
- Kim, B.-H. and K. Chun (2001). Fabrication of an electrostatic track-following micro actuator for hard disk drives using soi wafer. *Journal of Micromechanics and Microengineering*.
- Kobayashi, M. and R. Horowitz (2001). Track seek control for hard disk dual-stage servo systems. *IEEE Transactions on Magnetics* **37**, 949–54.
- Koganezawa, S., K. Takaishi, Y. Mizoshita, Y. Uematsu, and T. Yamada (1997). Development of integrated piggyback milli-actuator for high density magnetic recording. In: *International Conference on Micromechatronics for Information and Precision Equipment*. pp. 20–23.
- Kuwajima, H. and K. Matsuoka (2002). Thin film piezoelectric dual-stage actuator for hdd. In: *InterMag Europe, Session BS04*.
- Lee, S.-H., S.-E. Baek and Y.-H. Kim (2000). Design of a dual-stage actuator control system with discrete-time sliding mode for hard disk drives. In: *Proc. of the 39th IEEE Conference on Decision and Control*. pp. 3120–25.
- Li, Y. and R. Horowitz (2001). Mechatronics of electrostatic microactuator for computer disk drive dual-stage servo systems. *IEEE/ASME Transactions Mechatronics* **6**, 111–21.
- Li, Y. and R. Horowitz (2002). Design and testing of track-following controllers for dual-stage servo systems with pzt actuated suspensions [in hdd]. *Microsystem Technologies* **8**, 194–205.
- Lou, Y., P. Gao, B. Qin, G. Guo, E.-H. Ong, A. Takada and K. Okada (2002). Dual-stage servo with on-slider pzt microactuator for hard disk drives. In: *InterMag Europe, Session BS03*.
- Mizoshita, Y., S. Hasegawa and K. Takaishi (1996). Vibration minimized access control for disk drive. *IEEE Transactions on Magnetics* **32**, 1793–98.
- Mori, K., T. Munemoto, H. Otsuki, Y. Yamaguchi and K. Akagi (1991). A dual-stage magnetic disk drive actuator using a piezoelectric device for a high track density. *IEEE Transactions on Magnetics* **27**, 5298–300.
- Muller, L. (2000). *Ph.D. Dissertation: Gimballed Electrostatic Microactuators with Embedded Interconnects*. University of California. Berkeley, CA, USA.
- Nakamura, S., K. Suzuki, M. Ataka and H. Fujita (1999). An electrostatic micro actuator for a magnetic head tracking system of hard disk drives. In: *Transducers '97*. Chicago, IL, USA. pp. 1081–84.
- R.B. Evans, J.S. Griesbach and W.C. Messner (1999). Piezoelectric microactuator for dual-stage control. *IEEE Transactions on Magnetics* **35**, 977–81.
- Rotunno, M. and R.A de Callafon (2000). Fixed order H_∞ control design for dual-stage hard disk drives. In: *Proc. of the 39th IEEE Conference on Decision and Control*. pp. 3118–19.

- Sasaki, M., T. Suzuki, E. Ida, F. Fujisawa, M. Kobayashi and H. Hirai (1998). Track-following control of a dual-stage hard disk drive using a neuro-control system. *Engineering Applications of Artificial Intelligence* **11**, 707–16.
- Schroeck, S.J., W.C. Messner and R.J. McNab (2001). On compensator design for linear time-invariant dual-input single-output systems. *IEEE/ASME Transactions Mechatron.* **6**, 50–57.
- Semba, T., T. Hirano and L.-S. Fan (1999). Dual-stage servo controller for hdd using mems actuator. *IEEE Transactions on Magn.* **35**, 2271–73.
- Soeno, Y., S. Ichikawa, T. Tsuna, Y. Sato and I. Sato (1999). Piezoelectric piggy-back bicroactuator for hard disk drive. *IEEE Transactions on Magnetics* **35**, 983–87.
- Suh, S.-M., C.C. Chung and S.-H. Lee (2002). Design and analysis of dual-stage servo system for high track density hdds. *Microsystem Technologies* **8**, 161–68.
- Suzuki, T., T. Usui, M. Sasaki, F. Fujisawa, T. Yoshida and H. Hirai (1997). Comparison of robust track-following control systems for a dual stage hard disk drive. In: *Proc. of International Conference on Micromechatronics for Information and Precision Equipment*. pp. 101–18.
- Tomizuka, M. (1987). Zero phase error tracking algorithm for digital control. *Transactions of ASME, Journal of Dynamical Systems, Measurements, and Control* **109**, 65–68.
- Whilte, M. T. and W.-M. Lu (1999). Hard disk drive bandwidth limitations due to sampling frequency and computational delay. In: *Proc. of the 1999 IEEE/ASME International Conference on Intelligent Mechatronics*. pp. 120–25.
- Wongkomet, N. (1998). *Ph.D. Dissertation: Position Sensing for Electrostatic Micropositioners*. University of California, Berkeley, CA, USA.
- Yamaguchi, T. (2001). Modelling and control of a disk file head-positioning system. *Proceedings of the Institution of Mechanical Engineers, Part I (Journal of Systems and Control Engineering)* **215**, 549–567.

List of Figures

1	VCM actuator in a HDD.	36
2	VCM actuator in a HDD.	37
3	Electrostatic microactuators: Comb-drives vs. Parallel-plates	38
4	Differential parallel-plates actuators and electrical-isolation features	39
5	Capacitive position sensing. Comb-drives vs. Parallel-plates motion	40
6	Capacitive position sensing circuits. Synchronous scheme vs. Switched-capacitance scheme	41
7	Schematics of translational microactuator vs. rotary microactuator. Courtesy from Lilac Muller	42
8	Pico-slider mounted on a translational microactuator. Courtesy from Horsely 1998	43
9	A simplified schematic including driving and sensing circuits for the electrostatic microactuator. Courtesy from Wongkomet 1998	44
10	Open-loop and closed-loop frequency response of the prototype microactuator with a pico-slider. The capacitive position measurement (solid line) is compared to the measurements from LDV (dashed line). Courtesy from Naiuvudhi Wongkomet	45
11	Fabrication example 1: HexSil	46
12	Translational high-aspect ration microactuator	47
13	Basic silicon-on-insulator fabrication process	48
14	Electrostatic driving array of microactuator from SOI	49
15	Deep trench fabrication process adapted for backside release	50
16	Microactuator with integrated gimbal fabricated by ABR	51
17	Piezoresistive strain sensor on steel substrate	52
18	Disk drive servo control.	53
19	Master-slave design structure.	54
20	Decoupled control design structure.	55
21	PQ control design structure.	56
22	Parallel control design structure.	57
23	Dual-stage control plant.	58
24	Decoupled dual-stage control design block diagram.	59
25	The sensitivity block diagram.	60
26	Illustration of dual-stage sensitivity S_T design.	61
27	Self-tuning control of the MA.	62
28	μ -synthesis design block diagram.	63
29	(a) open loop Bode plot of the decoupled design; (b) open loop Bode plot of the μ -synthesis design; (c) closed loop sensitivity Bode of the decoupled design; (d) closed loop sensitivity Bode plot of the μ -synthesis design.	64
30	Control parameters adaptation response.	65
31	Dual-stage seek control design.	66
32	Dual-stage short span seek response.	67

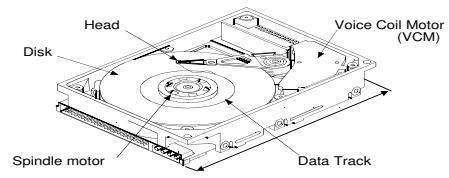


Figure 1: VCM actuator in a HDD.

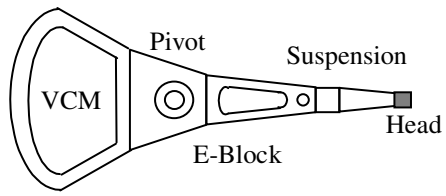


Figure 2: VCM actuator in a HDD.

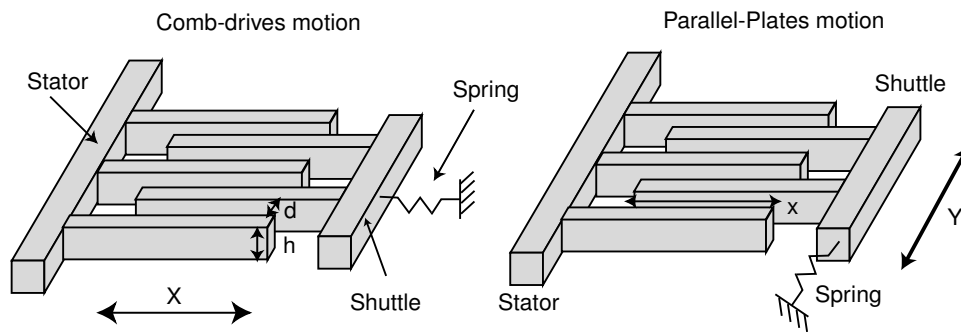


Figure 3: Electrostatic microactuators: Comb-drives vs. Parallel-plates

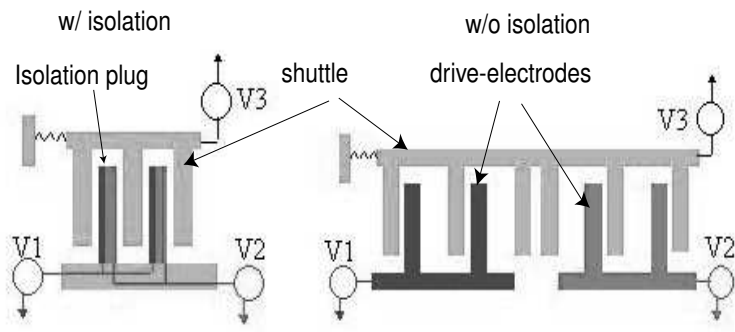


Figure 4: Differential parallel-plates actuators and electrical-isolation features

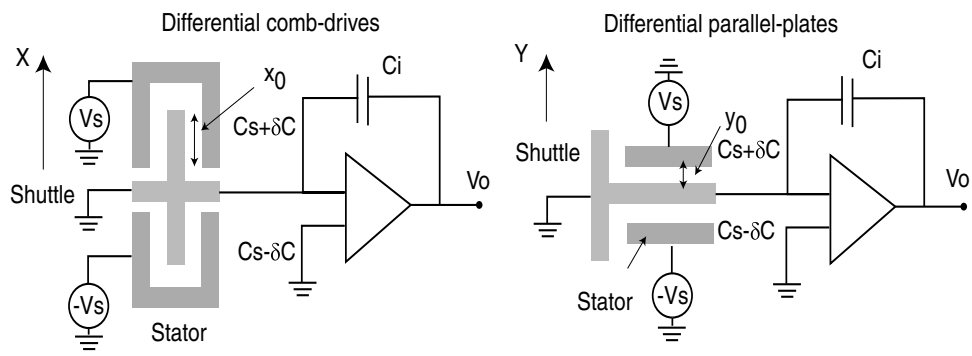


Figure 5: Capacitive position sensing. Comb-drives vs. Parallel-plates motion

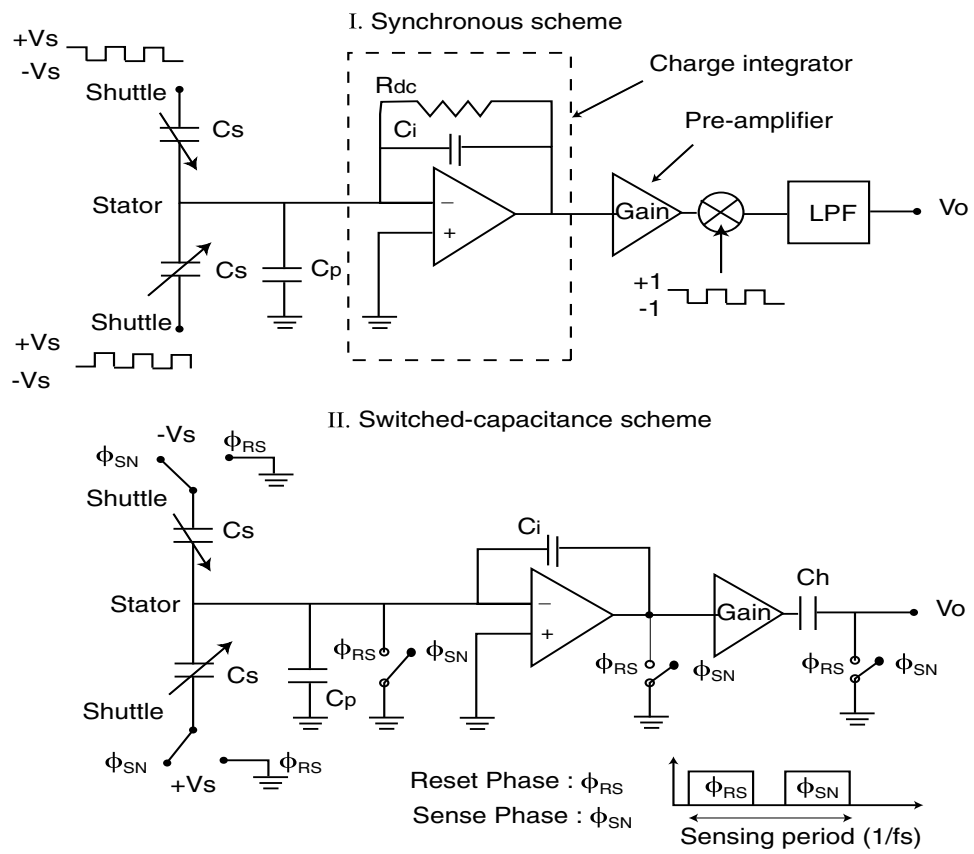


Figure 6: Capacitive position sensing circuits. Synchronous scheme vs. Switched-capacitance scheme

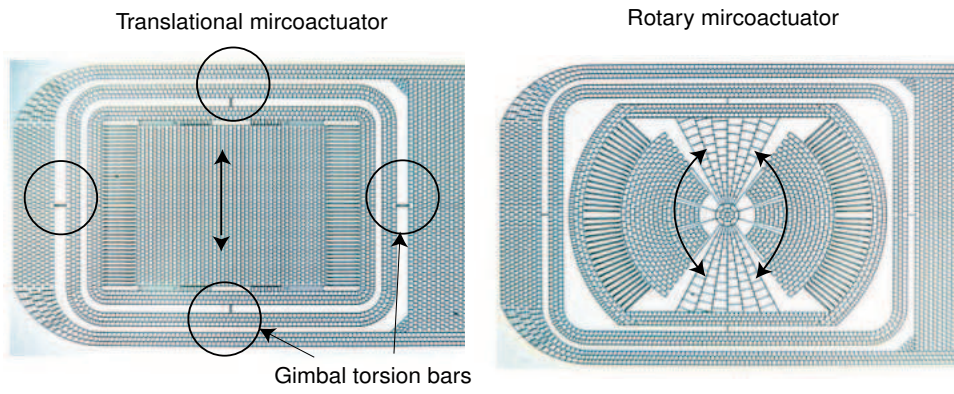


Figure 7: Schematics of translational microactuator vs. rotary microactuator. Courtesy from Lilac Muller

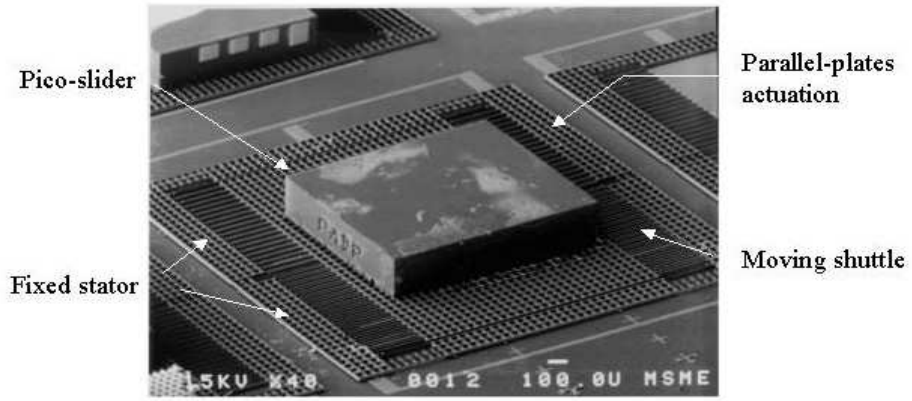


Figure 8: Pico-slider mounted on a translational microactuator. Courtesy from Horsely 1998

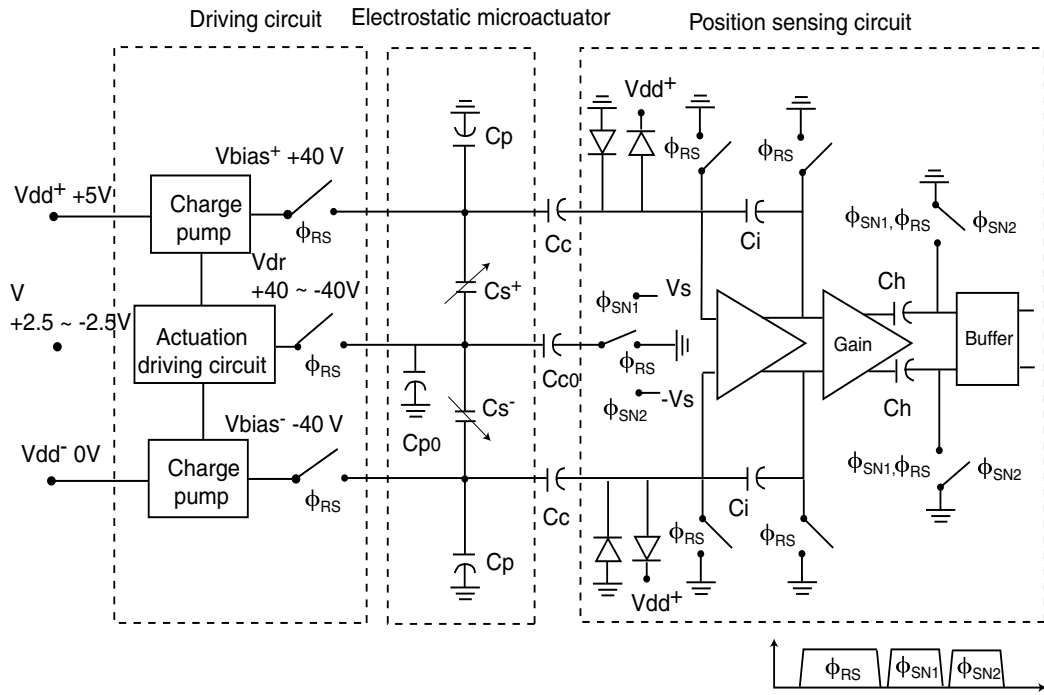


Figure 9: A simplified schematic including driving and sensing circuits for the electrostatic microactuator. Courtesy from Wongkomet 1998

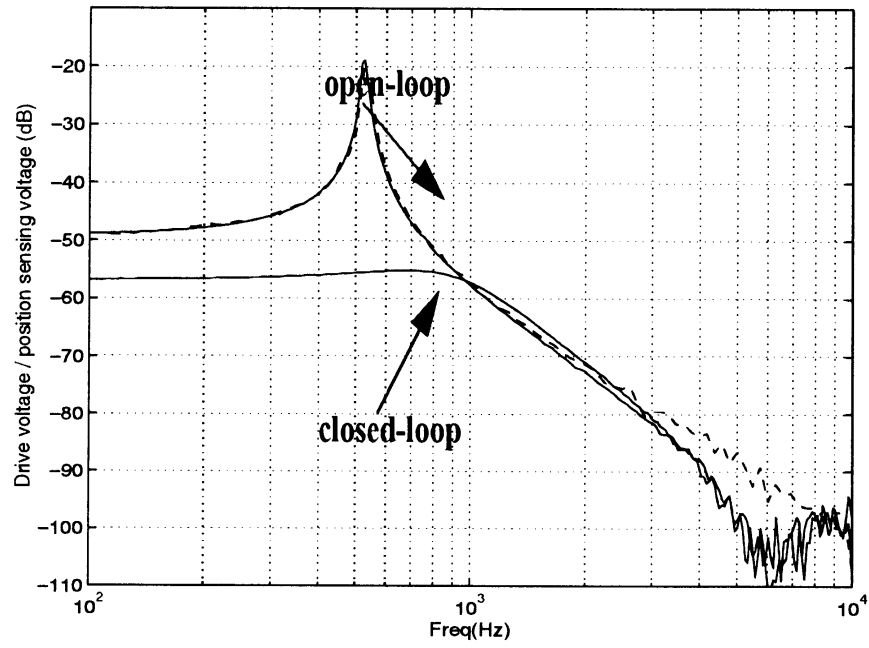


Figure 10: Open-loop and closed-loop frequency response of the prototype microactuator with a pico-slider. The capacitive position measurement (solid line) is compared to the measurements from LDV (dashed line). Courtesy from Naiuvudhi Wongkomet

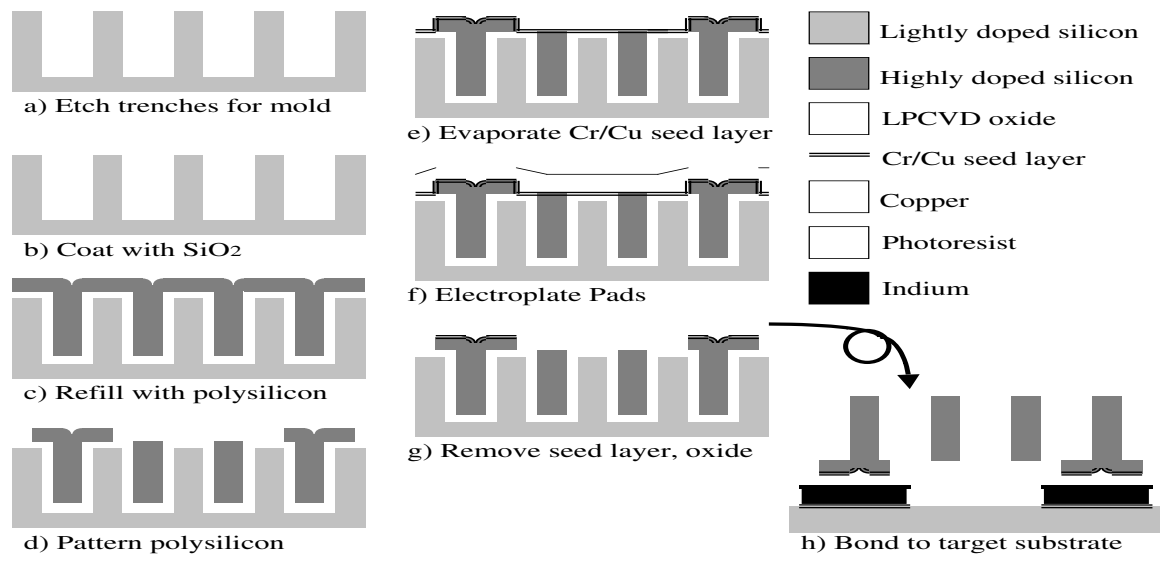


Figure 11: Fabrication example 1: HexSil

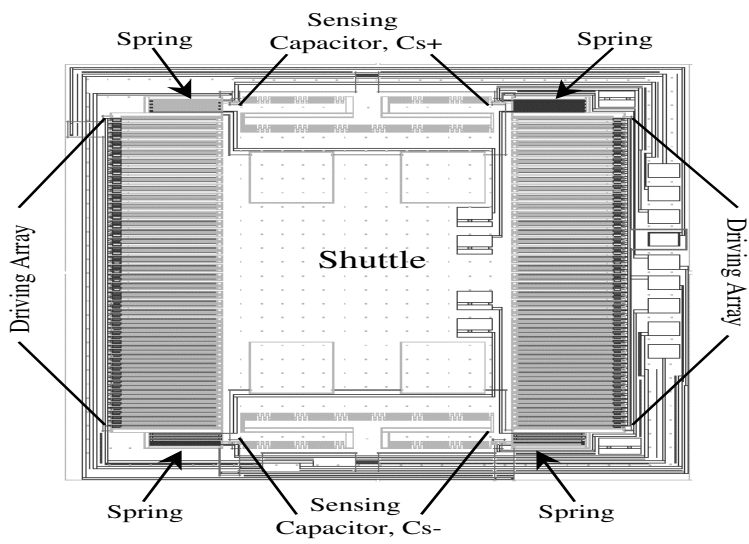


Figure 12: Translational high-aspect ration microactuator

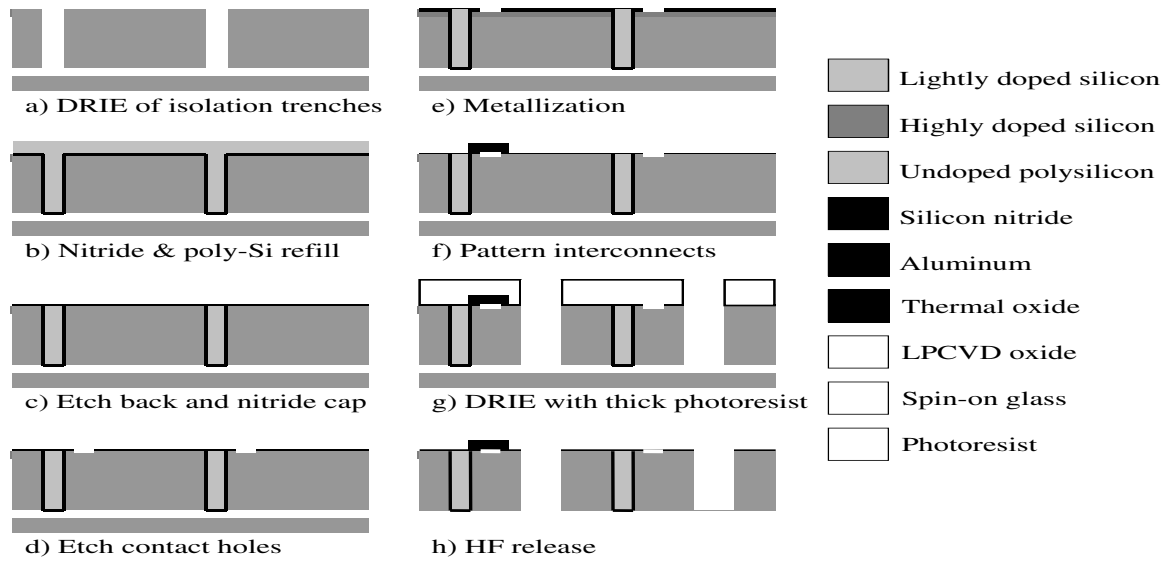


Figure 13: Basic silicon-on-insulator fabrication process

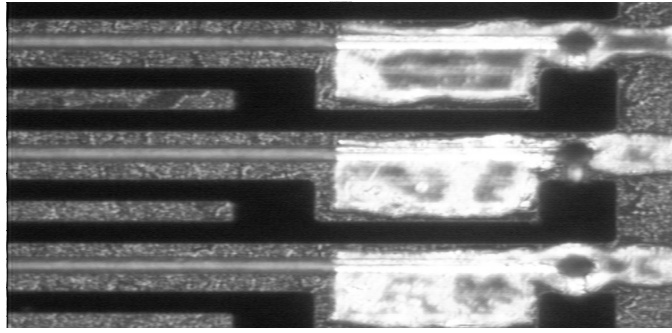


Figure 14: Electrostatic driving array of microactuator from SOI

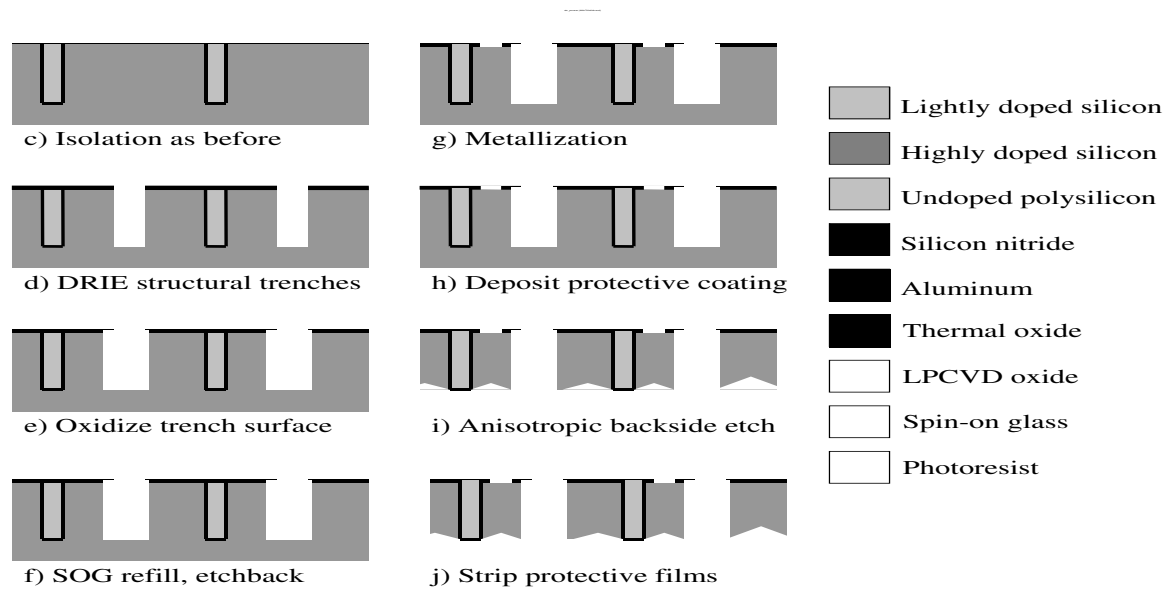


Figure 15: Deep trench fabrication process adapted for backside release

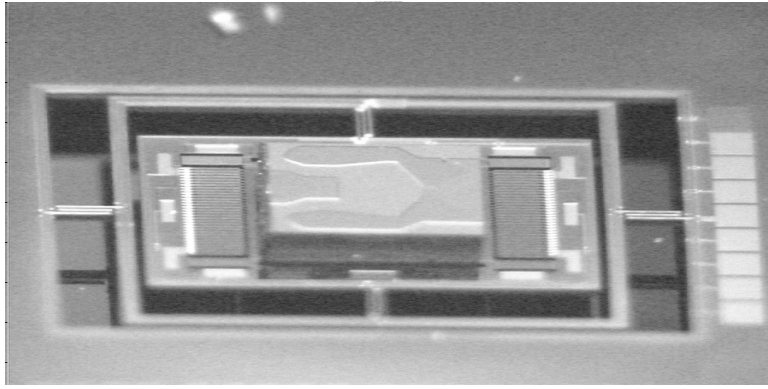


Figure 16: Microactuator with integrated gimbal fabricated by ABR

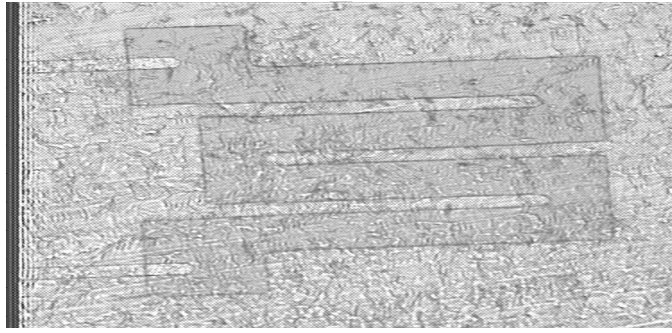


Figure 17: Piezoresistive strain sensor on steel substrate

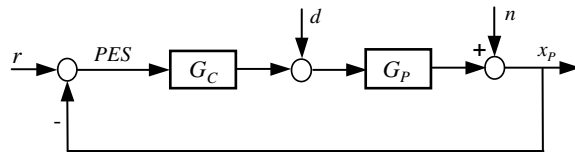


Figure 18: Disk drive servo control.

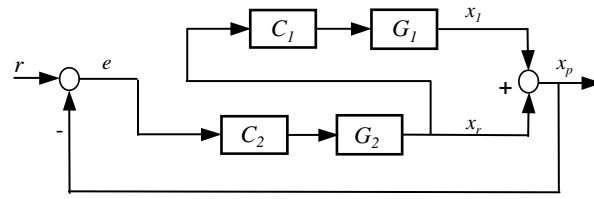


Figure 19: Master-slave design structure.

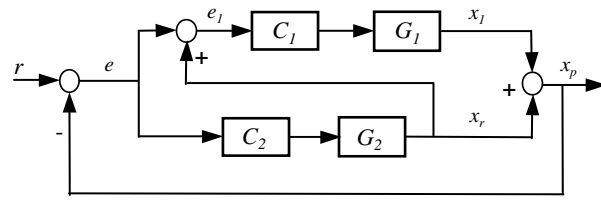


Figure 20: Decoupled control design structure.

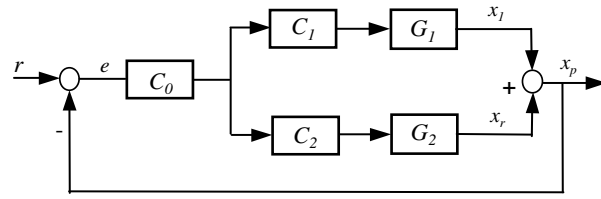


Figure 21: PQ control design structure.

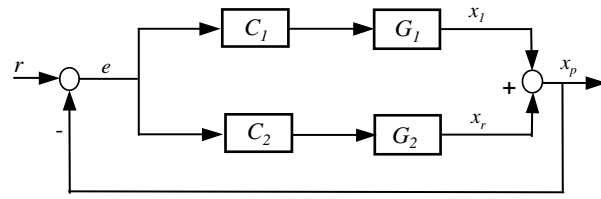


Figure 22: Parallel control design structure.

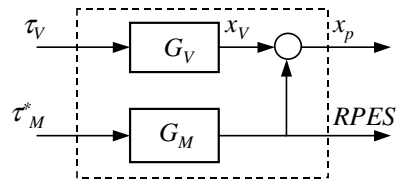


Figure 23: Dual-stage control plant.

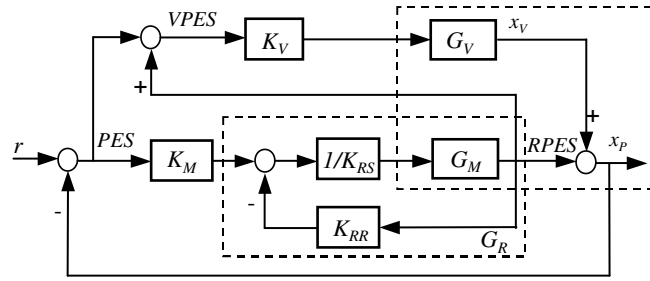


Figure 24: Decoupled dual-stage control design block diagram.

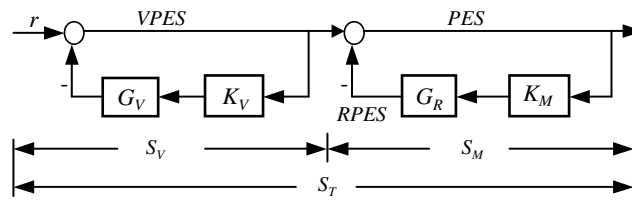


Figure 25: The sensitivity block diagram.

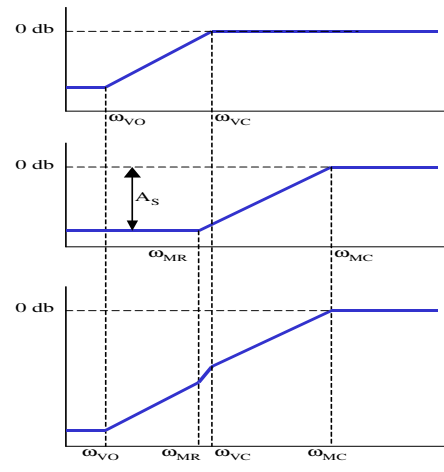


Figure 26: Illustration of dual-stage sensitivity S_T design.

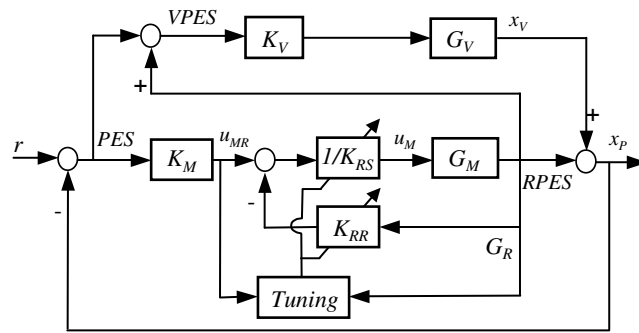


Figure 27: Self-tuning control of the MA.

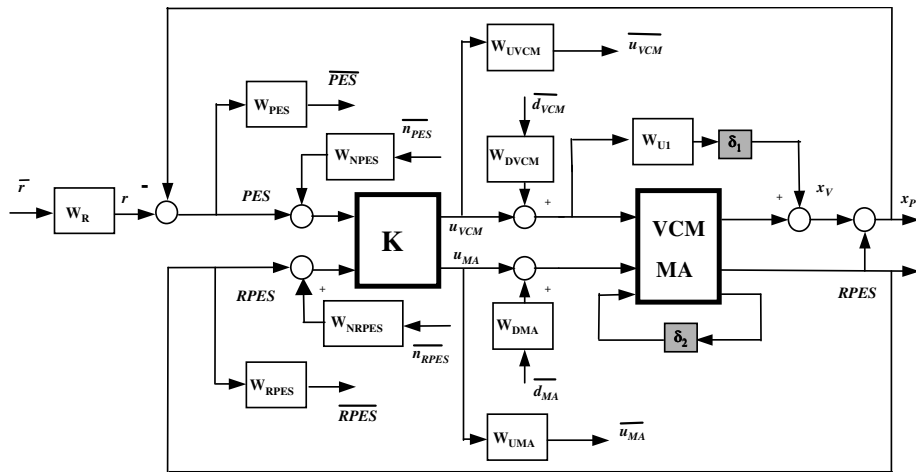
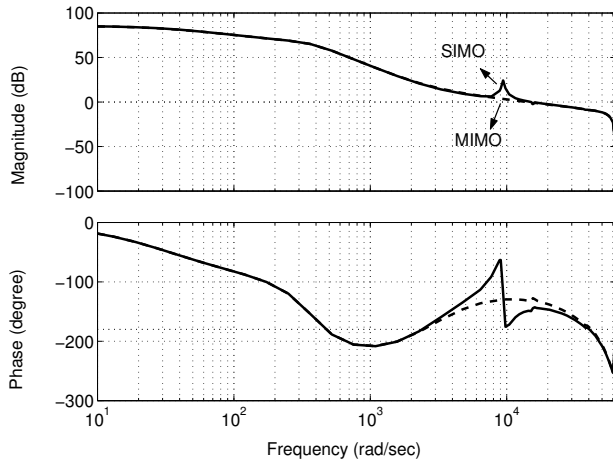
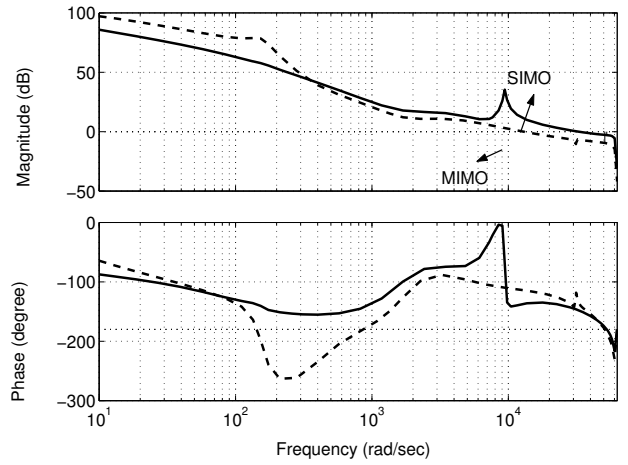


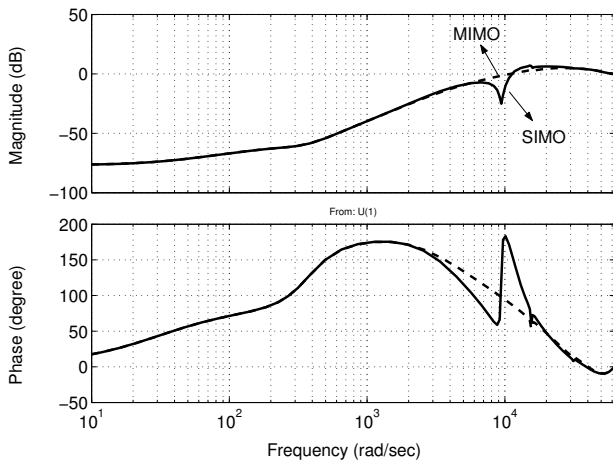
Figure 28: μ -synthesis design block diagram.



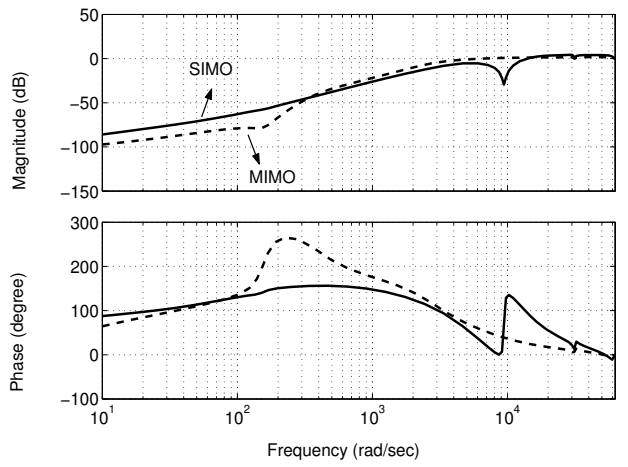
(a)



(b)



(c)



(d)

Figure 29: (a) open loop Bode plot of the decoupled design; (b) open loop Bode plot of the μ -synthesis design; (c) closed loop sensitivity Bode of the decoupled design; (d) closed loop sensitivity Bode plot of the μ -synthesis design.

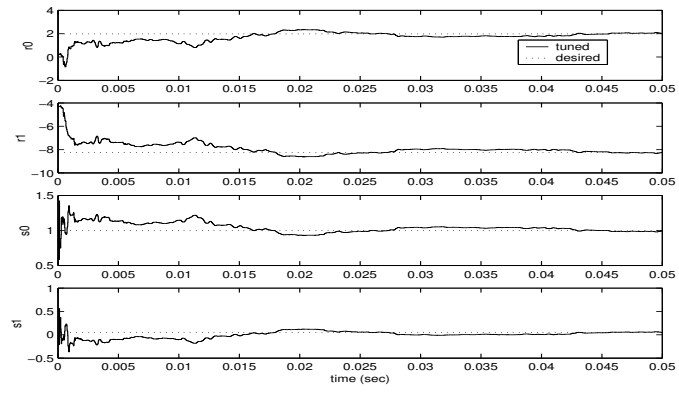


Figure 30: Control parameters adaptation response.

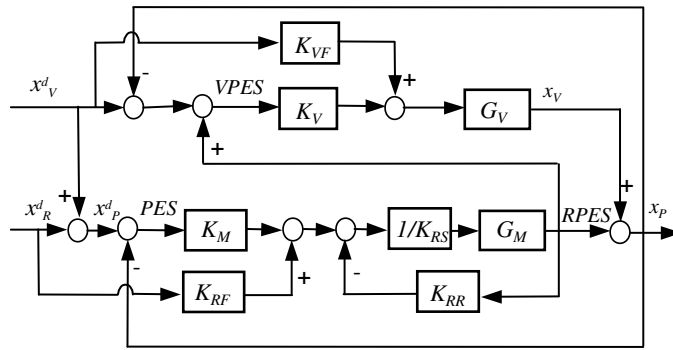


Figure 31: Dual-stage seek control design.

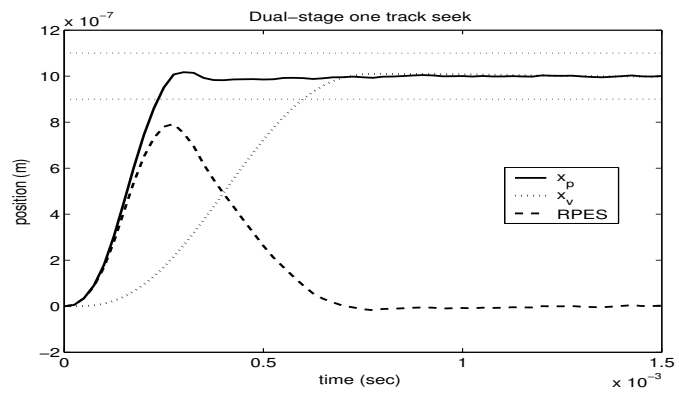


Figure 32: Dual-stage short span seek response.

List of Tables

1	Parameters of the electrostatic microactuator design by Horsley 1998	69
---	--	----

Parameters	Source*	Value
Nominal gap	D	10 μm
Structure thickness	D	45 μm
Rotor mass, m	I	44 μg
dC/dx	C	68 fF/ μm
Actuation voltage, bias voltage	D	40 V
Actuation voltage, maximum driving voltage	D	+/- 40 V
Voltage-to-force gain K_v	I	50 nN/V
Mechanical spring constant K_m	I	29 N/m
Electrostatic spring constant K_e	I	9.6 N/m
Damping coefficient, b	I	1.03×10^{-4} N/(m/s)
Voltage-to-position DC gain	M	0.05 $\mu\text{m}/\text{V}$
Resonance frequency, w_r	M	550 Hz

*: D=Design value, C=Calculation, M=Measurement, I=Inferred from measurements

Table 1: Parameters of the electrostatic microactuator design by Horsley 1998